

Photometric redshifts for the CFHTLS-Wide [★]

F. Brimiouille¹, M. Lerchster^{1,2}, S. Seitz^{1,2}, R. Bender^{1,2}, and J. Snigula^{2,1}

¹ Universitätssternwarte München, Ludwig-Maximilians Universität, Scheinerstr. 1, 81679 München, Germany

² Max-Planck-Institut für extraterrestrische Physik, Giessenbachstraße, 85748 Garching, Germany

Received; accepted

ABSTRACT

Aims. We want to derive bias free, accurate photometric redshifts for those fields of the Canada-France-Hawaii Telescope Legacy Survey (CFHTLS) Wide Data which are covered in the u^* , g' , r' , i' and z' filters and are public on January 2008. These are 21, 5 and 11 square degrees in the W1, W3 and W4 fields with photometric data for 1.397.545 (W1), 366.190 (W3) and 833.504 (W4) galaxies i.e. for a total of 2.597.239 galaxies.

Methods. We use the photometric redshift code PHOTO-z of Bender et al. (2001).

Results. To study the reliability of the photometric redshifts for the CFHTLS broad band filter set we first derive redshifts for the CFHTLS-Deep field D1, and compare the results to the spectroscopic and photometric redshifts presented in Ilbert et al. (2006). After that we compare our redshifts for the W1, W3 and W4 fields to about 7500 spectroscopic redshifts from the VVDS therein. For galaxies with $17.5 \leq i'_{AB} \leq 22.5$ the accuracies and outlier rates become $\sigma_{\Delta z/(1+z)} = 0.033$, $\eta \sim 2\%$ for W1, $\sigma_{\Delta z/(1+z)} = 0.037$, $\eta \sim 2\%$ for W3 and $\sigma_{\Delta z/(1+z)} = 0.035$, $\eta \sim 2.5\%$ outliers for W4 fields.

Finally we consider the photometric redshifts of Erben et al. (2008) which were obtained with exactly the same photometric catalog using the BPZ-redshift code and compare them with our computed redshifts. For the total galaxy sample with about 9000 spectroscopic redshifts from VVDS, DEEP2 or SDSS we obtain a $\sigma_{\Delta z/(1+z)} = 0.04$ and $\eta = 5.7\%$ for the PHOTO-z redshifts. We also merge the subsample with good photometric redshifts from PHOTO-z with that one from BPZ to obtain a sample which then contains 'secure' redshifts according to both the PHOTO-z and the BPZ codes. This sample contains about 6100 spectra and the photometric redshift qualities become $\sigma_{\Delta z/(1+z)} = 0.037$ and $\eta = 1.0\%$ for our PHOTO-z redshifts.

Conclusions. We conclude that this work provides a bias free, low dispersion photometric redshift catalog (given the depth and filter set of the data), that we have criteria at hand to select a 'robust' subsample with fewer outliers. Such a subsample is very useful to study the redshift dependent growth of the dark matter fluctuations with weak lensing cosmic shear analyses or to investigate the redshift dependent weak lensing signal behind clusters of galaxies in the framework of dark energy equation of state constraints.

The PHOTO-z photometric redshift catalog is provided on request. Send emails to fabrice@usm.lmu.de

Key words. Surveys – Galaxies: photometry – Galaxies: distances and redshifts – Galaxies: high redshift

1. Introduction

The CFHTLS Wide survey plans to image 170 square degrees in four patches of 25 to 72 square degrees through the whole filter set ($u^*g'r'i'z'$) down to $i' = 24.5$. This survey will (among other goals) allow to study the evolution of galaxies, the large scale structures as traced by galaxies, groups and clusters of galaxies. Due to its superb PSF-quality one can also directly study the line of sight matter distribution through weak lensing analysis. Full exploitation of the data requires the redshift of galaxies to be known in order to obtain the 3 dimensional arrangement of galaxies and to turn the observed galaxy colors into restframe properties. Obtaining spectra for millions of galaxies is impossible at the moment. The photometric redshift

technique, however, can provide redshifts for large numbers of faint galaxies with an accuracy that eg. allows galaxy evolution studies or 3D lensing analysis. For high quality photometric redshifts the photometry should cover a wide wavelength range. The necessary wavelength range has to be adapted to the depth of the survey. For a survey as shallow as SDSS, NIR data are not essential since basically all redshifts are low ($z < 1$), and there are hardly any SED- z degeneracies. This holds as long as U-band data are available, which locate the Balmer or 4000 Angstrom break; therefore, the central wavelength of the U-band (or in general, the bluest) filter determines the redshift above which photometric redshifts are trustable (see Gabasch et al. 2007 and Niemack et al. 2008 for the impact of GALEX data on photoz-accuracies). The CFHTLS-Wide (W1-W4) and Deep surveys are deeper than SDSS, which implies that larger redshifts but also smaller absolute luminosities and thus different SED-types are traced. In this situation SED- z degeneracies can occur (eg. degeneracies between a redshift $z = 0.7$ emission line galaxy and a 'normal' $z = 1.2$ galaxy) which can be cured either with bluer U-band (from space) or with NIR data. The classical 'catastrophic' failures become really relevant only in data as deep or deeper than the CFHTLS-Deep fields. Only in data as deep as this there is a significant number of galaxies with sufficiently high redshifts where Lyman break and 4000 Angstrom might be misidentified. This effect could be suppressed

Send offprint requests to:

F. Brimiouille e-mail: fabrice@usm.lmu.de

[★] Based on observations obtained with MegaPrime/MegaCam, a joint project of CFHT and CEA/DAPNIA, at the Canada-France-Hawaii Telescope (CFHT) which is operated by the National Research Council (NRC) of Canada, the Institut National des Sciences de l'Univers of the Centre National de la Recherche Scientifique (CNRS) of France, and the University of Hawaii. This work is based on data products produced at TERAPIX and the Canadian Astronomy Data Centre (CADCC) as part of the Canada-France-Hawaii Telescope Legacy Survey, a collaborative project of NRC and CNRS.

Table 1. CFHTLS Wide Fields: location

ID	RA (J2000)	Dec (J2000)
W1	02:18:00	-07:00:00
W2 ^a	08:54:00	-04:15:00
W3	14:17:54	+54:30:31
W4	22:13:18	+01:19:00

^a We will provide photozs for this field later

with absolute luminosity priors, and (almost) avoided with NIR data.

The principle disadvantage of photometric redshifts is the relatively low redshift resolution (due to the width of filters) compared to spectroscopic redshifts. On the other hand, photometric redshifts have turned into a vital tool in resolving redshift ambiguities where spectra show single (emission) line features only (Lilly et al. 2006).

In the Erben et al. (2008) we combined publicly available¹ $u^*g'r'i'z'$ data, remapped and coadded the frames, derived an i' -band detected photometric catalog; we also made pixel based data and the photometric catalog public. This catalog also contains a photometric redshift estimate obtained with the BPZ-code (Benítez et al. 2000), using the original CWW-templates and redshift priors developed from Benítez for the HDF. The redshifts suffer a bias for $z < 1.0$, where low redshift galaxies are at too high redshift and high redshift galaxies are at too low redshifts. Also, it was emphasized in Erben et al. (2008) that photometric redshifts in this catalog are not trustable above redshifts of $z = 1.4$. Providing redshifts with strongly reduced bias is the main goal of this paper: In section 2 we briefly summarize our previous work. We then describe the spectroscopic data that we use for calibration and for redshift accuracy tests in section 3. We shortly describe the photometric redshift method of Bender et al. (2001) and our relative zeropoint recalibration method in section 4. In section 5 we demonstrate that this redshift code is bias free and works as good as the method of Ilbert et al. (2006) by comparing to spectroscopic and photometric redshift results of Ilbert et al. for the CFHTLS D1 field. We then present photometric redshifts for the W1, W3 and W4 fields, and infer their quality (as a function of SED type and brightness) from spectroscopic data in these fields. Our redshifts are then compared to the previous ones from Erben et al. (2008). We also empirically correct for their redshift bias. We end up with two sets of photometric redshifts, which can also be used in combination, to select a subsample with most reliable redshifts.

2. Data Acquisition, Reduction and Photometric Catalogs

Here we briefly review the data acquisition, the data reduction steps and the creation of the multicolor catalogs; more details can be found in Erben et al. (2008).

The data used in this analysis are taken in the framework of the synoptic CFHTLS-Wide observa-

¹ We are very grateful for the CFHTLS survey team to conduct the survey, and for the Terapix team (<http://terapix.iap.fr/>) for developing software, for preprocessing the images and carrying out the numerous data control steps. A description of the CFHTLS survey can be found at <http://www.cfht.hawaii.edu/Science/CFHTLS>

tions with the MegaPrime instrument mounted at the Canada-France-Hawaii Telescope (CFHT). See <http://www.cfht.hawaii.edu/Science/CFHTLS/> and <http://terapix.iap.fr/cplt/oldSite/Descart/summarycfhtlswi> for further information on survey goals and survey implementation. We consider all Elixir processed CFHTLS-Wide fields with observations in all five optical bands $u^*g'r'i'z'$ which are publicly available. After downloading all data from CADC we further process them with our GaBoDS/THELI pipeline (astrometric solution, remapping, stacks). The stacked data have a pixel size of $0.186''$, a typical PSF of $0.8''$ and limiting AB-magnitudes of about 24.5 (5σ within a $2''$ aperture for a point source) in the i' -band.

For the creation of the multicolor catalogs we first cut all images in the filter $u^*g'r'i'z'$ of a given field to the same size. We then measure the seeing in each band and convolve all images with a Gaussian to degrade the seeing to that of the worst band.

For object detection we use SExtractor in dual-image mode with the unconvolved i' -band image as the detection image. We measure the fluxes in apertures in the convolved images and obtain aperture colors. The aperture we use for photoz estimates has a diameter of $1.86''$. It is important to keep track of locations which have increased photometric errors that are not accounted for in the SExtractor flux errors. These are: halos of very bright stars, defraction spikes of stars, areas around large and extended galaxies and various kinds of image reflections. Masks are automatically generated but then finalized by human eye. These masks can also be used as masks where shape estimates are unreliable, and they can be obtained from Erben et al. (2008) on request. We generate photometric redshifts for all objects. They have a non-zero-flag (equal to the MASK value in Erben et al. 2008) if photometry and thus redshifts (and possibly also shape estimates) could not be trustable. The fraction of flagged objects/area is about 20 percent. This is in line with conservative flagging, e.g., in previous work (compare Ilbert et al. 2006).

3. Spectroscopic Redshifts

The CFHTLS Wide fields W1 and W4 have a good spectroscopic coverage: Le Fèvre et al. (2004) and (2005) have released a catalog of 8981 spectra of galaxies, stars and QSOs with $17.5 < i_{AB} < 24.0$ in the VVDS 0226-04 field (which is located within the W1-field). The spectroscopic redshifts are within $0 < z < 5$, with a median redshift of about 0.76. The sample covers 0.5 deg^2 of sky area. For the CFHTLS W4 there are 17928 spectra of galaxies, stars and QSOs (Le Fèvre et al. 2004, 2005, Garilli et al. 07) located in the VVDS-F22 field with a magnitude limit of $i_{AB} < 22.5$. This sample covers 4 deg^2 of sky area.

The online database gives access to the redshifts and quality flags, to the multi-wavelength photometric information, as well as to the images and VIMOS spectra. The data can be accessed via the CENCOS² web tool.

The CFHTLS W3 has public spectroscopic data from the DEEP survey³ (Davis et al. 2003, 2007; Vogt et al. 2005; Weiner et al. 2005). The DEEP1 redshift catalog⁴ contains 658 objects with

² <http://cencosw.oamp.fr/EN/index.en.html>

³ Data presented herein were obtained at the W. M. Keck Observatory, which is operated as a scientific partnership among the California Institute of Technology, the University of California and the National Aeronautics and Space Administration. The Observatory was made possible by the generous financial support of the W. M. Keck Foundation.

⁴ <http://mingus.as.arizona.edu/~bjw/papers/>

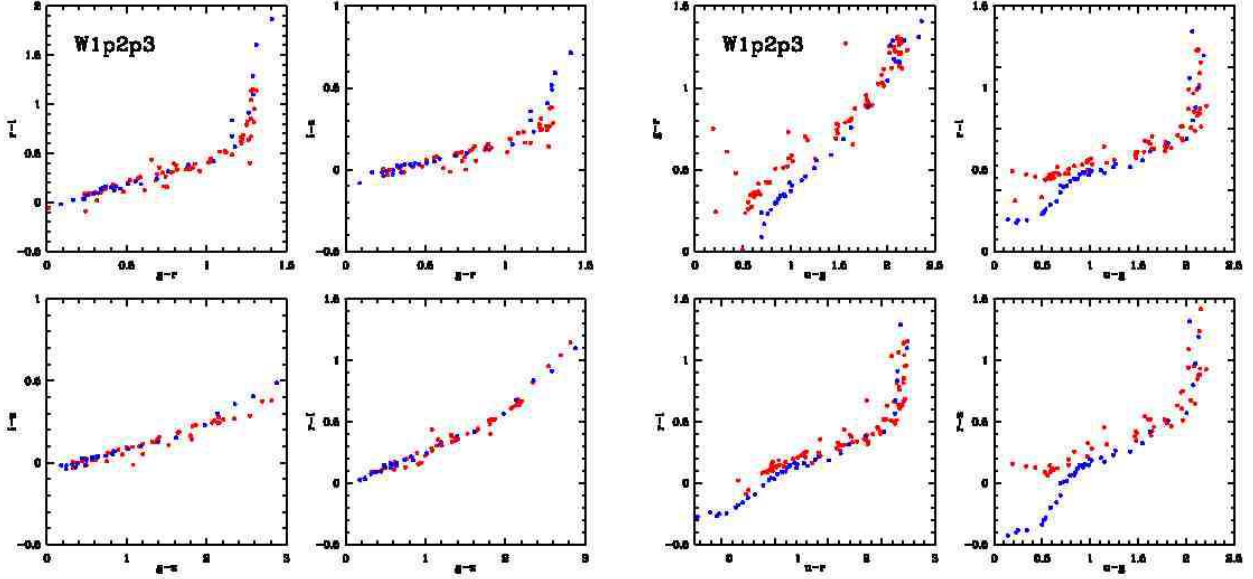


Fig. 1. Color-Color diagrams of stars (red dots), plotted against the Pickles (1998) stellar library (blue dots), on the field W1p2p3. Note, that all colors that do not contain a u^* -flux perform well. The potential reasons for the mismatch of u^* -band data are discussed in the text. To obtain these color-color diagrams, a significant shift (-0.20 mag) in u^* -flux was applied, the shifts for the other bands ($g'r'i'z'$) were 0.00, 0.00, -0.06 and 0.13 magnitudes.

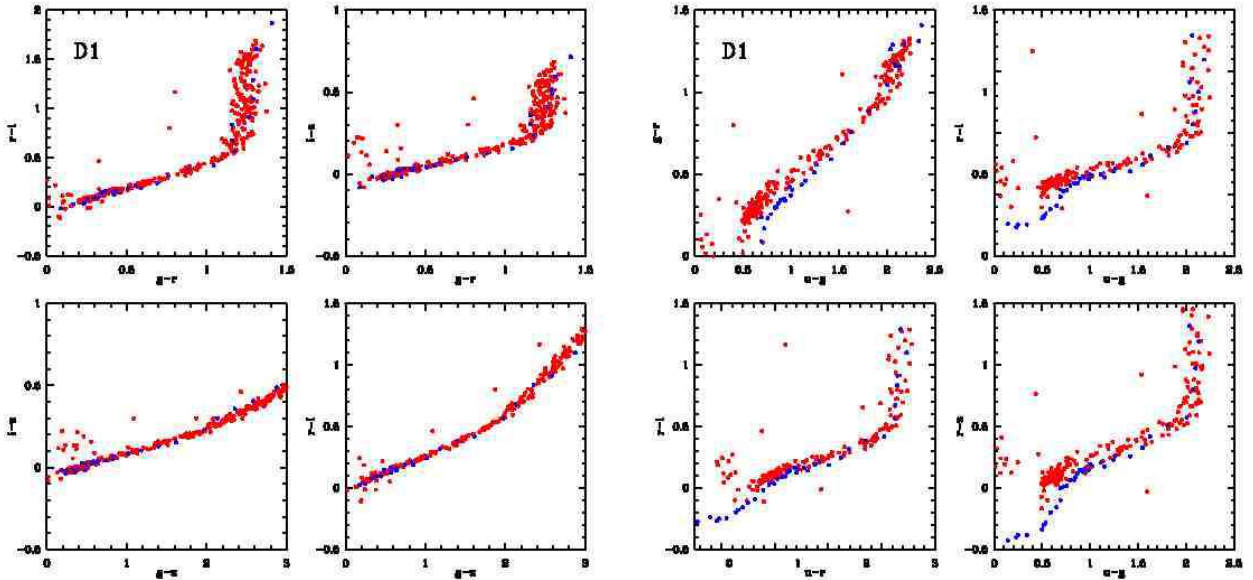


Fig. 2. CFHTLS D1 field: color-color diagrams of stars (red dots), plotted against the Pickles (1998) stellar library (blue dots), on the field D1. Note, that all colors that do not contain a u^* -flux perform well. To obtain this color-color diagram, a significant shift (-0.25 mag) in u^* -flux was applied, the shifts for the other bands ($g'r'i'z'$) were -0.06 , 0.00, -0.10 and 0.04 magnitudes.

a median redshift of $z = 0.65$. The DEEP2 DR3 redshift catalog⁵ contains 47700 unique objects with redshifts > 0.7 and covers 4 regions, each $120' \times 30'$ large. The targets were selected from the CFHT12K BRI imaging, eligible DEEP2 targets have $18.5 \leq R_{AB} \leq 24.1$. The region on the Groth Survey Strip, with $120' \times 15'$ has an overlap to the CFHTLS W3 field.

For the comparison to photometric redshifts we consider galax-

ies with trustworthy (for the W1 and W4 $\geq 95\%$, for the W3 $\equiv 100\%$) spectroscopic redshifts only. Due to low S/N (at high redshift) and the limited wavelength ranges of the spectra only 2933 objects on the CFHTLS W1, 410 objects on the CFHTLS W3 and 3688 objects on the CFHTLS W4 could be considered. In Fig. 8 we compare the photometric redshift distribution with the VVDS spectroscopic redshift distribution. The agreement is very good.

Our data from patches W3 and W4 have complete SDSS cover-

⁵ http://deep.berkeley.edu/DR3/zcat.dr3.v1_0.uniq.dat

age⁶, from patch W1 only southern pointings W1p4m0, W1p3m0 and W1p1m1 have SDSS overlap. Via the flexible web-interface SkyServer⁷ of the Catalog Archive Server (CAS), we get access to the spectra catalog.

For our purpose we only consider objects clearly classified as galaxy and a redshift trustworthy $\geq 95\%$. By matching the SDSS catalog with our photometric catalog we end up with 39 objects on the CFHTLS W1, 180 objects on the CFHTLS W3 and 309 objects on the CFHTLS W4. In total there are 528 objects with the spectroscopic redshift from the SDSS (Adelman-McCarthy et al. 2007).

4. Photometric redshift method and photometric calibration of CFHTLS Wide and Deep data

We use the PHOTO-z code of Bender et al. (2001) (see also Gabasch et al. 2004 about the construction of SED templates). The code calculates for each SED the full redshift likelihood function including priors for redshift and absolute luminosity. The stepsize for the redshift grid is equal to 0.01. Our aim in this paper is to estimate photometric redshifts from the optical bands of the CFHTLS-Wide data based on approved SED-templates and prior settings from earlier publications. The SEDs and priors used for this work are the same as in Bender et al. (2001) and Gabasch et al. 2004. Development of new SED-templates adapted to the CFHTLS data, application of better adjusted priors and further investigations, data from near infrared bands will be part of an upcoming paper (Lerchster et al. in prep.). Generally, our priors are weak and do hardly influence the result. The luminosity prior deals the fact that the absolute luminosity of galaxies are limited and do not exceed a certain value. It is flat over a broad range of restframe luminosities with a suppression of absolute Magnitudes brighter than -25 and fainter than -13 by a factor of 2 in probability at these luminosity values. The relatively strongest prior is the redshift prior for old stellar populations. The redshift prior considers that certain SED-Types do not exist at higher redshifts, it suppresses e.g. the probability for elliptical galaxies at a redshift of 0.8 by a factor of 2. We choose a prior which makes red SED types at $z = 0.6$ and S0-like galaxies at $z = 1$ one fifth as likely as at $z = 0.1$. The redshift priors for other SED types are almost flat. The redshift of the highest probability among all SEDs becomes the ‘photometric redshift’ of the object. The redshift ‘error’ of the object is obtained as

$$\Delta z_{\text{phot}} = \sqrt{\sum_{i,j} (z_i - z_{\text{max}})^2 \cdot P_{ij}}, \quad (1)$$

where the sum runs over all (discrete) redshifts z_i , and all SEDs and P_{ij} is the contribution of the j -th SED to the total (normalized) probability function at redshift z_i . Hence, the meaning of the ‘error’ is how well the galaxy is locatable in redshift space around the ‘best’ redshift. Sometimes, the redshift probabilities have a maximum at another distinct redshift (where so called ‘catastrophic outliers’ could arise). The potential redshift-SED-degeneracy can be read off in the chi-squares of the most likely

and the second most likely SED (which in general is different from the redshift likelihood ratios).

They could be improved with the now available, much larger spectroscopic and photometric datasets. This is subject of future work and will allow to further improve the photometric redshift accuracy.

The photometric calibration of the data is very important. Small errors in the photometric zero-points or false assumptions on the wavelength dependent transmission of the system (sky, telescope optics, filters, CCDs) have to be avoided or corrected. As throughput of the system we use the filter curves in <http://www1.cadc-ccda.hia-ihp.nrc-cnrc.gc.ca/community/CFHT/> These include optics (wide field corrector, image stabilizing plate, camera window), the mirror (approximated with the reflectivity of freshly aluminium coated glass) and the CCDs (QE is given only between 350 and 1000 nm). For the atmospheric extinction we used <http://www.cfht.hawaii.edu/Instruments/ObservatoryManual/> (for the blue optical part) where extinction is featureless. This wavelength dependent extinction shifts the effective wavelength of the filters to the red (relevant for the u^* -band, where it implies a shift of about 20 Angstroms).

With these ingredients we calculate the location of the Pickles stellar library stars (Pickles 1998) in color-color diagrams and compare them with colors of observed stars. The observed comparison stars are selected in the central region of the frames using their SExtractor CLASS_STAR and SExtractor flag parameters. We derive their aperture colors (after seeing matched convolution). An example is shown in Fig.1: red dots are used for measured stellar colors, and blue dots are used for the Pickles library stars. Stellar sequences are well located and can evidently be used to measure relative zeropoint offsets.

Our $u^* - r'$ vs $r' - i'$ diagram looks very different from that of Erben et al. (2008), where the stars show a huge scatter in $u^* - r'$ colors for large values of $r' - i'$. We show only the brightest (unsaturated) stars with highest SExtractor CLASS_STAR values, which implies that photometric errors are very small for stars in our diagrams. This then allows, to measure relative zeropoint offsets and to see whether the spread of stellar colors and the shape of the color-colors diagrams also agrees with expectations from stellar libraries for the assumed system throughput.

The $r' - i'$ vs $g' - r'$ diagram of observed and library stars has a very strong curvature at $g' - r' = 1.2$. This implies, that one can adjust the zeropoint offsets of the g' and i' -bands relative to the r' -band very well. If this is done one can proceed with the z' -band, using, e.g. the $g' - z'$ colors. In this way one gets zeropoints, for which stars have colors consistent to the Pickles library. After these adjustments g' , r' and i' band data usually match the expected curve very well. For z' -band data one might expect larger ‘scatter’ around the Pickles points, because some fields do show considerable amount of fringes, which can lead to systematic (relative to the fringe pattern) magnitude offsets for some of the stars. We finally also show all examples which involve u^* -band data. They don’t match the Pickles stars, since they occupy a larger interval in the $u^* - g'$ color (which can’t be fixed by a zeropoint offset, obviously). Since the $g' - r'$ color is corrected for zeropoint offsets already, it means, that stars, which are blue in $g' - r'$ are bluer than predicted in $u^* - g'$ for $u^* - g' < 1.7$ than expected. This could be explained by the fact that stars targeted by CFHTLS are more metal poor than those in the solar neighbourhood and therefore bluer in the UV. Alternatively, if throughput is the explanation, it would surprisingly imply that the throughput in the blue parts of the

⁶ Funding for the SDSS and SDSS-II has been provided by the Alfred P. Sloan Foundation, the Participating Institutions, the National Science Foundation, the U.S. Department of Energy, the National Aeronautics and Space Administration, the Japanese Monbukagakusho, the Max Planck Society, and the Higher Education Funding Council for England. The SDSS Web Site is <http://www.sdss.org/>;

⁷ <http://cas.sdss.org/astro/en/tools/search/SQS.asp>

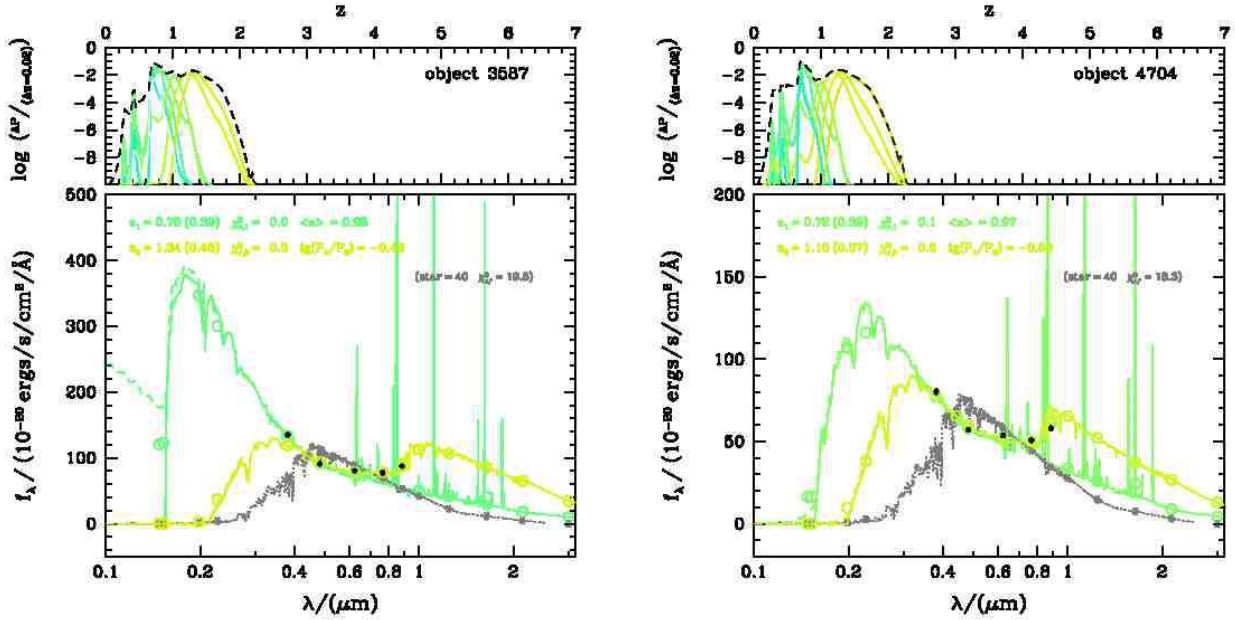


Fig. 3. Two examples for the SED-redshift degeneracy if optical bands only are used: One cannot disentangle a ‘normal’ galaxy at $z \approx 1.2$ from a heavily starforming blue galaxy at $z \approx 0.7$ which contributes significantly with its emission lines in the z-band. These ‘blue’ galaxies are faint and occur only in relatively deep data. The spectroscopic redshifts of the galaxies in the left and right panels are $z = 1.363$ (obj3587) and $z = 1.175$ (obj4704).

u^* -band has been underestimated; this does not appear very likely. On the other hand, if the mismatch of colors is due to metal poor stars (UV-excess), then the effect might have shown up more strongly in the deeper FORS Deep Field (Gabasch et al. 2004), where more of the halo is traced, and where the U-band filter curve is considerably bluer. As long as one cannot firmly identify the reason for this stretch in the $u^* - g'$ color, one could claim that it is not obvious, whether a ‘good’ stellar color-color diagram involving u^* -band data should match the Pickles colors at the blue or red end (or somewhere else). Furtheron difficulties in measuring the transmission function of the CFHT- u^* are well known, as several versions of the transmission curve can be found in the web which additionally complicates the analysis. The effect described above shows up in any CFHT u^* -band data we investigated (DEEP and WIDE fields), independent of the applied reduction pipeline but not in other fields we previously investigated (e.g. ESO DPS, in particular GOODS-S, compare Gabasch et al. 2004). Nevertheless, any remaining systematic effects leading to systematic errors in the zeropoint offset determination can be detected and corrected by calibrating the zeropoints using spectroscopic redshifts. We therefore looked into subfields with spectroscopic data (we took W1p2p2, W1p2p3, W4m0m0, W4m0m1, W4m0m2, W4p1m0, W4p1m1, W4p1m2, W4p2m0, W4p2m1, W4p2m2) and investigated how the color-color diagrams (involving u^* -band) looked like when photometric and spectroscopic redshifts matched well. It turned out, that a slight shift to the color-color diagrams of stars relative to that which matches the stars at the red end and which is shown in Fig. 1 was necessary, for all the fields, and that this shift was consistent in size from field to field. We took that as a description how observed stars have to look relative to the Pickles library, and calibrated other fields without spectroscopic data like that. We have tested how good this empiric photometric ZP-calibration works in the fields where we predicted the photometric redshifts based on the ‘ideal empirical color-color

diagram’ and compared to available spectroscopic data (this was done for the fields W3m1m2, W3m1m3 using DEEP2 spectra and for many subfields of W1, W3 and W4 using SDSS redshifts).

5. Photometric Redshifts: Accuracy tests with the CFHTLS D1 data

5.1. Results for the complete sample

We had been testing our photoz-method previously on the FDF, GOODS, MUNICS and COSMOS fields (Gabasch et al. 2007, 2006, 2004, Feulner et al. 2006, 2005; Gabasch et al. 2004 and Drory et al. 2001). Since any photometric redshift method is likely to fail if the system throughput is misunderstood, we first test our method on the CFHTLS D1 subfield, which has many spectra from the VVDS 0226-04 field, and where photometric redshifts have been derived by Ilbert et al. (2006) before. For the photometry of this deep field we use the $u^*g'r'i'z'$ science data from the T0003-release (including their weight and mask frames)⁸. We then obtain photometric catalogs in the same way as described before. For the spectroscopic sample we use all matchable spectra which fulfill the redshift quality criteria defined in Section 3. The match of spectroscopic and photometric redshifts is quantified the same way as in Ilbert et al. (2006), i.e., we define the outlier fraction and redshift accuracy of non-outliers as:

$$\eta = \text{fraction of outliers with } |z_{\text{spec}} - z_{\text{phot}}| / (1 + z_{\text{spec}}) > 0.15 \quad (2)$$

$$\sigma_{\Delta z / (1+z)} = 1.48 \times \text{median}(|z_{\text{spec}} - z_{\text{phot}}| / (1 + z_{\text{spec}}))_{\text{non-outliers}}. \quad (3)$$

⁸ We would like to thank the terpix team for reducing and releasing these data.

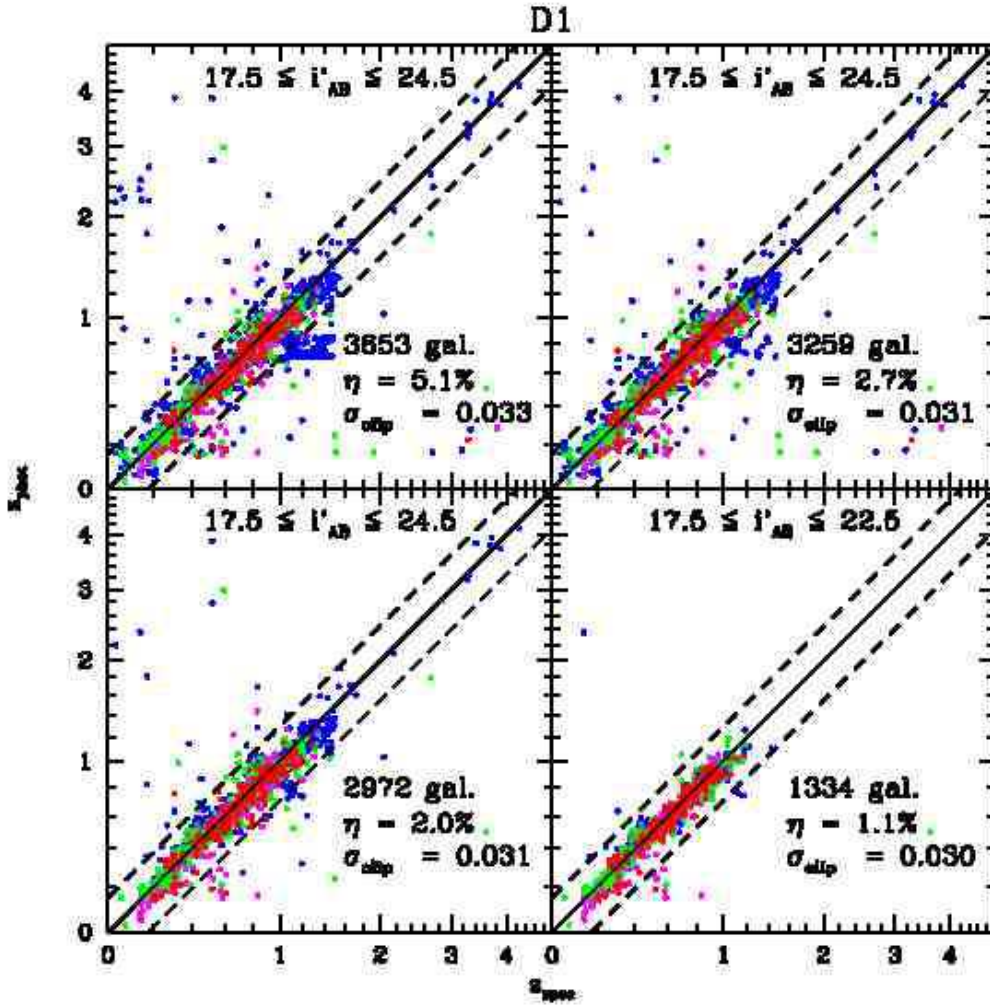


Fig. 4. PHOTO- z photometric redshifts against spectroscopic redshifts for the CFHTLS D1 field. Left upper panel: all non-stellar objects (stars are excluded by morphology and SED-fit). Upper right panel: All objects from the left, but without most likely SEDs corresponding to starforming galaxy with strong emission lines, which this excludes objects where a SED-phot z degeneracy is known (see text for more details). Left lower panel: as above, but now also excluding also those objects where the width of the redshift probability distribution at the most likely redshift is large, $\Delta z_{\text{phot}z} > 0.25 * (1 + z_{\text{phot}z})$. Right lower panel: as before, but restricting the object sample to $17.5 \leq i'_{AB} \leq 22.5 \text{ mag}$. The color coding is: red symbols for SEDs that describe elliptical galaxies and S0s, blue symbols for blue, strongly star forming galaxies, the magenta and green coded objects are for SEDs that form a continuous sequence between the red and blue galaxies in terms of color and star forming activity.

This definition of $\sigma_{\Delta z/(1+z)}$ is quite different from the 'true' dispersion

$$\sigma = \sqrt{\frac{\sum_i^{N_{\text{spec}}} (z_{i,\text{phot}z} - z_{i,\text{spec}})^2}{(N_{\text{spec}} - 1)}} \quad , \quad (4)$$

since it describes only the typical redshift deviation within a narrow range around the true value. We recommend to also consider σ in parallel to $\sigma_{\Delta z/(1+z)}$ and η , since this tells how 'off' outliers typical are. Also, if one compares the performance of photometric redshifts with optical data alone to the case where eg. NIR data are added, it usually happens that η and σ decrease, whereas $\sigma_{\Delta z/(1+z)}$ can even increase, since more data points end in the 'almost true' section, but the median deviation within this $|z_{\text{spec}} - z_{\text{phot}z}| / (1 + z_{\text{spec}}) < 0.15$ interval can increase. Nevertheless, one would, for many application prefer the situation with reduced η and σ , even if σ_{clip} is slightly

increased. Using these definitions from above, our fraction of outliers for the D1 field is $\eta \sim 5\%$ and the accuracy becomes $\sigma_{\Delta z/(1+z)} = 0.033$. This accuracy has to be compared to that of Ilbert et al. (2006). They have obtained redshifts with the LePHARE code using about 70 template SEDs, which have been optimized with spectroscopic-photometric data in the D1 field. The photometry comes from the CFHTLS Deep1 with integration times of about 11h, 7h, 17h, 37h and 17hours in the $u^*g'r'i'z'$ -filters and PSFs between 1.1 and 0.9 arcseconds (as released in the Terapix T0003 release) and the BVRI-VVDS with integration times of 3 to 7 hours in the CFH12K BVRI filters and median PSF of 0.8" -0.9" (as described in McCracken et al. 2003). The 50 percent point source completeness is at AB magnitudes of 26.5, 26.4, 26.1, 25.9 and 25.0 for the $u^*g'r'i'z'$ -filters and 26.5, 26.2, 25.9 and 25.0 for the BVRI-filters according to Ilbert et al. (2006). So, their VVDS data are fairly deep in the B and V filters, and we therefore expect a gain in the photometric

redshift accuracies, when these data are used: The VVDS B- and V-filters can sample breaks that are within the very broad CFHTLS-g' filter, and the R-band helps to locate breaks that are within either the CFHTLS-r' and i'-filters. In addition to the optical data Ilbert et al. (2006) could use deep J and K band data for 13% of their objects. Their results for D1 are released at at http://terapix.iap.fr/rubrique.php?id_rubrique=227. They reached values of $\sigma_{\Delta z/(1+z)} = 0.029$ and $\eta = 3.8\%$ using all their photometric data and galaxies with $i < 24$ according to their paper. This result is surprisingly close to our result if one accounts for the denser wavelength coverage and the fractional coverage with NIR data.

5.2. Creating subsamples with higher photo-z precision

We now explore whether we can identify a subsample of galaxies with more precise photometric redshifts. One expects that the quality of photometric redshifts varies with the SED properties of the galaxies. Using optical bands ($u^*g'r'i'z'$) only, there is a redshift range where strongly starforming galaxies cannot be discriminated from 'more normal' galaxies at other redshifts. In Fig. 3 we show the photometric redshift probability distribution for two spectroscopic objects, and the SED-fit for the most likely and second most likely SED. One can see that without near infrared data (e.g., J or H-band) the SED-photoz degeneracy cannot be broken. In both cases the true redshift is that of a 'normal' galaxies, without strong emission lines. Since at the depth of the survey we do not expect very many strongly starforming galaxies anyhow, we decided to reject galaxies for which the strongly starforming SEDs is formally most likely. In this way we get rid of the 'systematic arms' in the spec-z photoz plots; the accuracy becomes $\sigma_{\Delta z/(1+z)} \approx 0.031$ and the outlier rate is $\eta = 2.7\%$. If we further exclude objects with photometric redshift errors $\Delta_z \text{photoz} > 0.25 * (1 + z_{\text{photoz}})$ the remaining accuracy and fraction of outliers become $\sigma_{\Delta z/(1+z)} = 0.031$ and $\eta \sim 2\%$. The fraction of galaxies that we loose with these selection criteria (small width of the most likely redshift, and excluding galaxies with SEDs degenerate to strongly starforming ones) is about 20 percent. We nevertheless provide photozs for all redshifts and flag galaxies with likely imprecise redshifts. The meaning of the photometric redshift flag values can be looked up in the Table A.1 in the Appendix.

Finally, if we limit the magnitudes of catalog to $i'_{AB} \leq 22.5$ mag, which corresponds to the limiting magnitude of the primary targets of the spectroscopic survey on the VVDS-F22 field, this leads to an accuracy of $\sigma_{\Delta z/(1+z)} = 0.030$ and the fraction of catastrophic outliers is $\eta \sim 1\%$.

We now more directly compare the performance of our photometric redshifts with that of Ilbert et al. (2006). We retrieve their photometric redshift catalog⁹, and merge our spectro-photometric-redshift sample with their photometric redshift. This 'merged' sample is now smaller than our spectro-photometric-redshift sample alone, since we skip sources that have more than one photometric-redshift counterpart within the search radius in the Ilbert et al. (2006) catalog. Table 2 and Fig. 5 show, that if one takes all spectroscopic objects in the merged sample of the PHOTO-z and LePHARE catalogs, the clipped dispersions and the outlier rates are similar ($\sigma_{\Delta z/(1+z)} = 0.033$, $\eta = 4.6\%$ and $\sigma_{\text{clip}} = 0.028$, $\eta = 4.3\%$ for the PHOTO-z and LePHARE code respectively), whereas the true dispersion of PHOTO-z is significantly smaller than that of the LePHARE

⁹ We would like to thank the authors for providing their photometric redshift catalog to the public.

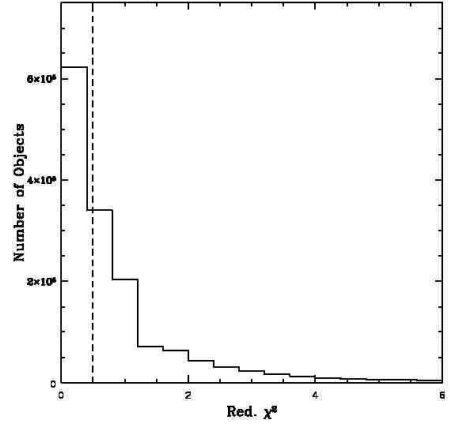


Fig. 6. Histogram of the reduced χ^2 for all galaxies in the CFHTLS Wide field W1 as obtained for the best fitting template and redshift. The dotted vertical line indicates the median reduced χ^2 of 0.5.

catalog ($\sigma = 0.138$ vs $\sigma = 0.187$). It also shows, that using SED-filtering and photometric redshift error filtering (for the PHOTO-z case) and photometric redshift error filtering (for the LePHARE case –note, that we don't make use of the full probability function but just of the redshift range, including 68% of the redshift probability when defining 'good objects' as $(z_{\text{sup-68}} - z_{\text{inf-68}}) \leq 0.25 (1 + z_{\text{phot}})$ for the LePHARE catalog) reduces the outlier rate for both cases. The stronger decrease of outliers in the PHOTO-z case (1.8% vs 3.9%) is also caused by the effect that more objects are filtered out when defining a 'good object catalog', relative to the LePHARE catalog, as can be seen from the sample size. To see how photometric redshifts compare for objects which are considered as 'good' objects in both catalogs, we define a catalog of 'common good objects' and compare their photometric redshift quality in Table 2 as well. For common good objects, the outlier rate and the true dispersion is smaller using PHOTO-z redshift, whereas the clipped sigma is slightly smaller for LePHARE photometric redshifts. However the PHOTO-z redshifts show a small systematic effect compared to the LePHARE ones, as the redshifts seem to slightly oscillate around the 45 degree line. Whether this effect might be cured by optimizing the SED-templates for the CFHT filters will be investigated in an upcoming paper (Lerchster et al. in prep.), but one should keep in mind that the LePHARE redshifts are more immune against these oscillations since they do not use only the CFHT- $u^*g'r'i'z'$ data but also include the CFH12K $BVRI$ data and in addition partly NIR data (J and K). If one derives photometric redshifts for large area surveys, one will not have a spectroscopic sample to compare with; however comparing the redshift results and the assignments of 'good or secure photometric redshift objects' will improve the selection of a robust sample with few outliers.

6. Photometric Redshifts in the CFHTLS "Wide Fields" W1, W3 and W4

We obtain photometric redshifts after zeropoint calibration as described before. A comparison between spectroscopic (VVDS sample only) and photometric redshifts for the CFHTLS Wide Field W1 and W4 is shown in Fig. 9. The outlier fraction is $\eta \leq 4\%$. In Fig. 7 we show the distribution of the redshift errors on CFHTLS Wide field W1 using the VVDS spectra. The er-

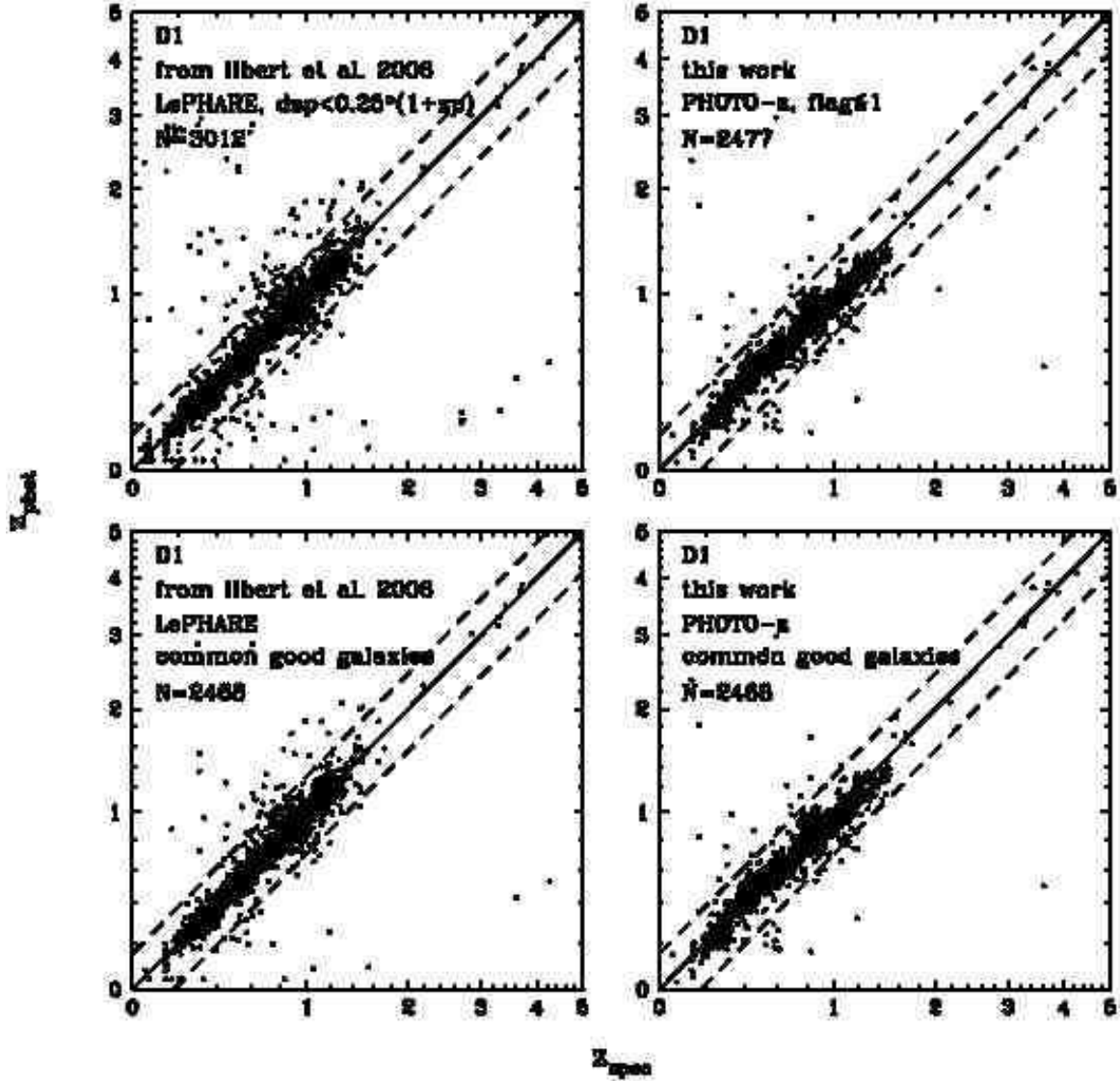


Fig. 5. This Figure compares the photometric redshifts derived by Ilbert et al. (2006) with LePHARE (two left panels) with those derived with PHOTO-z in this work (two right panels). The upper plot shows the photometric redshifts for objects which are characterized as ‘good’ ($dzp := z_{\text{sup-68}} - z_{\text{inf-68}} \leq 0.25(1 + z_{\text{phot}})$) in the LePHARE catalog and ($\Delta z_{\text{photoz}} < 0.25 * (1 + z_{\text{photoz}})$ & excluding strongly starforming SED-types) in the PHOTO-z catalog. The lower two panels show photometric redshifts for those objects which are both in the ‘good’ LePHARE and ‘good’ PHOTO-z sample.

ror distribution is only gaussian in its center, which has a width of 0.038 equal to the ‘clipped width’, $\sigma_{\Delta z/(1+z)}$ defined by Ilbert et al. (2006). The outliers are too many to be compatible with such a narrow gaussian; the true dispersion is equal to 0.08 (for galaxies with VVDS spectra in the W1-field)

Fig. 6 presents the χ^2 distribution of the best fitting templates and photometric redshifts for all the objects. The median value of the reduced χ^2 is 0.5 which implies that the galaxy templates describe the galaxies rather well.

6.1. Tests of the zeropoint calibration method

We now investigate how well our empirical calibration of zeropoints using the color-color diagram of stars works. We derive zeropoints offset from matching the color-color diagram of

stars as learned in the W1 and W4 subfields fields with VIMOS spectroscopic data. This offsets are used in the photoz code. We then compare our photometric redshifts to 410 galaxies from the Deep survey (Weiner et al. 2005; Davis et al. 2007) in the CFHTLS W3 field (which cover areas different from the VIMOS galaxies). The photometric redshift prediction for these Deep galaxies is accurate to $\sigma_{\Delta z/(1+z)} \sim 0.041$ with an outlier rate of $\eta \sim 6\%$.

Since our data (partly) overlap with the Sloan Digital Sky Survey (SDSS), we can compare the photozs to spectroscopic ones for further 528 galaxies from the SDSS DR6. These low redshift objects give an accuracy of $\sigma_{\Delta z/(1+z)} \sim 0.036$ and a outlier rate of only 1/528. When we finally combine the DEEP2 and the SDSS DR6 spectra we determine an accuracy of $\sigma_{\Delta z/(1+z)} \sim 0.045$ and an outlier rate of $\eta \sim 1.5\%$ for the combined sample, see Fig. 10.

Table 2. Photometric redshifts of PHOTO-z and LePHARE in the CFHTLS D1 field are compared to the spectroscopic sample consisting of VVDS spectroscopic data (there are no SDSS or DEEP2 spectra). In this table, σ denotes the ‘true’ dispersion, without clipping outliers, and $\sigma_{\Delta z/(1+z)}$ denotes the width of the distributions after clipping outliers (as defined in equations 3 and introduced by Ilbert et al. 2006). The photometric redshifts of PHOTO-z were obtained with CFHTLS data only, the LePHARE redshifts also make use of the VVDS BVRI imaging data and (for 13 percent of objects) also of NIR data.

Code	Sample: CFHTLS-D1	$N_{z_{\text{spec}}}$ ¹⁰	Median error	Mean error	σ	$\sigma_{\Delta z/(1+z)}$	η [%]
PHOTO-z	all PHOTO-z objects	3035	-0.011	-0.006	0.138	0.033	4.6%
PHOTO-z	good PHOTO-z objects	2477	-0.010	-0.006	0.082	0.031	1.8%
PHOTO-z	common good objects	2468	-0.010	-0.006	0.082	0.031	1.7%
LePHARE	all LePHARE objects	3035	-0.003	0.015	0.187	0.028	4.3%
LePHARE	good LePHARE objects	3012	-0.003	0.013	0.173	0.028	3.9%
LePHARE	common good objects	2468	-0.003	0.004	0.099	0.029	2.6%

The definitions of the samples are:

all PHOTO-z objects: $z_{\text{spec}} > 0, z_{\text{PHOTO-z}} > 0$

good PHOTO-z objects: $z_{\text{spec}} > 0, z_{\text{PHOTO-z}} > 0$, SED-type filtering, photometric redshift error filtering $\Delta z_{\text{photoz}} < 0.25 (1 + z_{\text{photoz}})$

common good objects: $z_{\text{spec}} > 0, z_{\text{PHOTO-z}} > 0$, SED-type filtering, photometric redshift error filtering for both codes

all LePHARE objects: $z_{\text{spec}} > 0, z_{\text{LePHARE}} > 0$

good LePHARE objects: $z_{\text{spec}} > 0, z_{\text{LePHARE}} > 0$, photometric redshift error filtering $((z_{\text{sup-68}} - z_{\text{inf-68}})) \leq 0.25 (1 + z_{\text{phot}})$

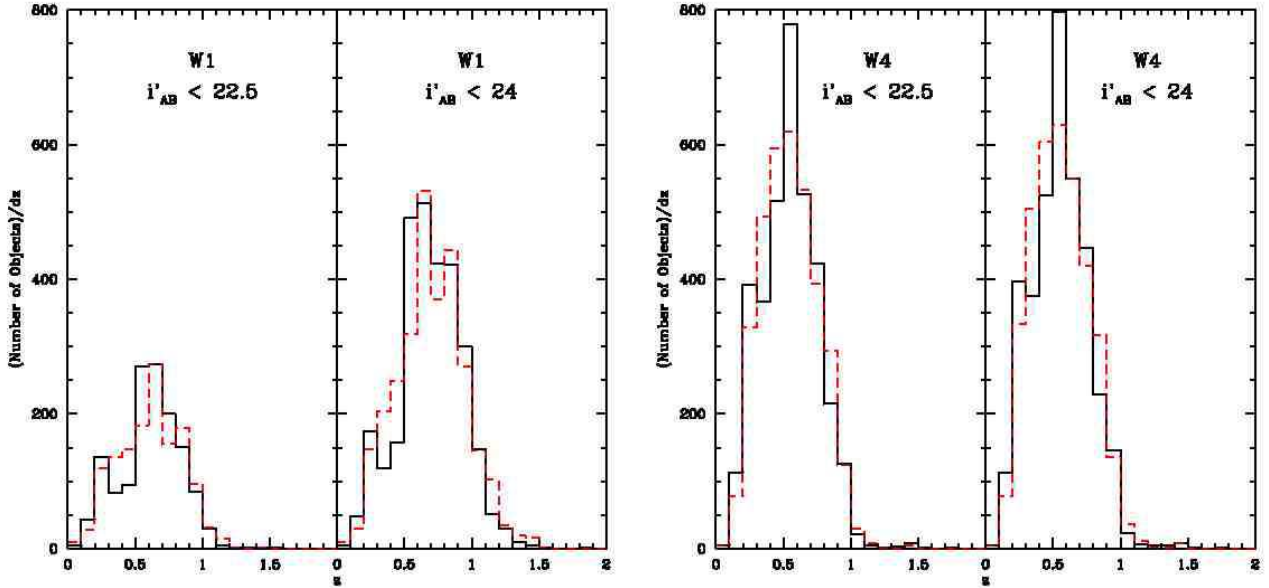


Fig. 8. Photometric and spectroscopic (VVDS) redshifts in the CFHTLS W1 (left) and the W4 (right) fields. Left panels: sample with $i \leq 22.5$. Right panels: sample with $i' \leq 24.5$. The black lines are for photometric redshifts and the red lines are for spectroscopic ones, which come from the VVDS sample.

We think, that this shows, that our photometric calibration method can be applied to all CFHTLS Wide fields.

We show in Fig. 11 how the photometric redshifts change if we use for the zeropoint calibrations stars only (instead of galaxy redshifts, see Fig. 9 for that case). Results are shown for the CFHTLS W1 field and the CFHTLS W4 field. The accuracy deteriorates from $\sigma_{\Delta z/(1+z)} = 0.035$ ($\sigma_{\Delta z/(1+z)} = 0.038$) to $\sigma_{\Delta z/(1+z)} = 0.04$ ($\sigma_{\text{clip}} = 0.044$) for the field W4 (W1), the outlier rate roughly stays the same.

6.2. Redshift accuracies as a function of type & brightness

In Fig. 12 we compare the photometric redshifts to the spectroscopic redshifts for different apparent magnitude intervals for the CFHTLS W1 and W4 fields. The fraction of catastrophic outliers

η increases from 2.7 % to 9.7 %, going from $17.5 \leq i'_{AB} \leq 21.5$ up to $23.5 \leq i'_{AB} \leq 24.5$, this has been also seen by Ilbert et al. (2006).

Fig. 13 shows the photometric redshifts versus the spectroscopic redshifts for different spectral types for the CFHTLS W1 and W4 field. We sort the SEDs we use to describe galaxies into 4 groups. The first one contains SEDs that describe ellipticals and S0s and is colored red in plots, the fourth contains very blue, strongly starforming SEDs (colored blue in plots) and the third (magenta) and fourth (green) group form a continuous sequence of SEDs in color and star forming activity between the first and fourth group of galaxy-SEDs. The accuracies of the photometric redshifts become $\sigma_{\Delta z/(1+z)} \sim 0.037$ for group one and two (red and magenta), and $\sigma_{\Delta z/(1+z)} \sim 0.044$ for group three and four (green and blue). The catastrophic outliers increase by a factor of about

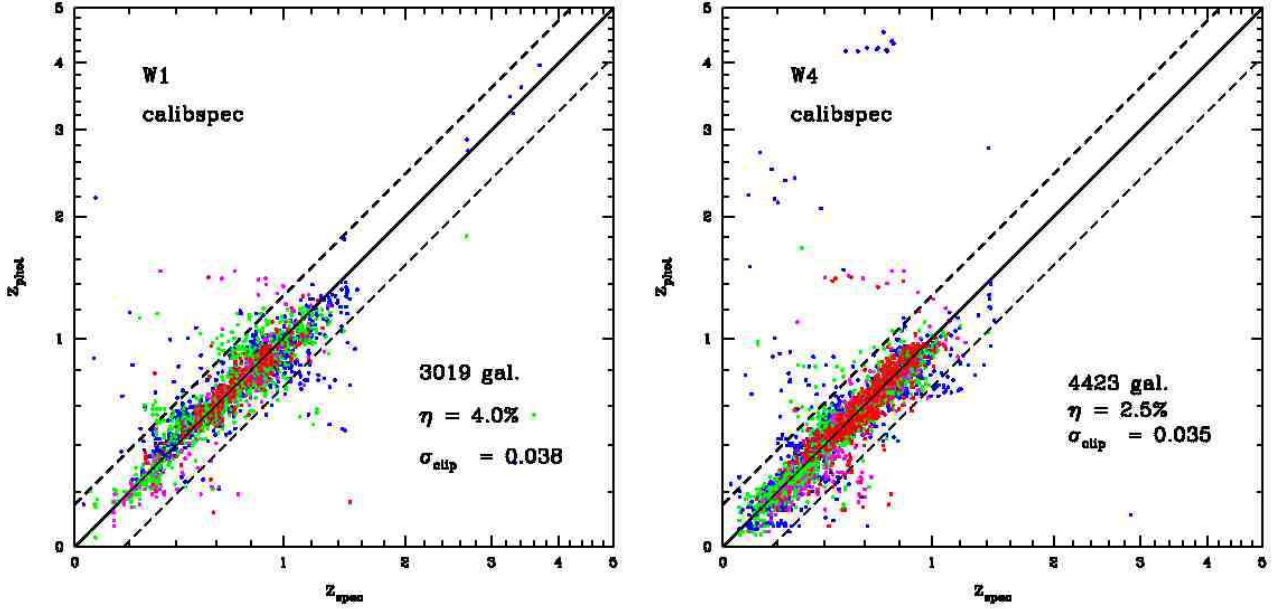


Fig. 9. PHOTO-z photometric redshifts against spectroscopic ones for the CFHTLS W1(left) and W4 (right) field. SED types are color-coded: red for E/S0 galaxy types, blue for strongly star forming, blue galaxies, magenta and green symbols are for SEDs that form a continuous sequence of SEDs in color and star forming activity between the red and blue galaxies. The cyan symbols are for SEDs bluer than those coded with magenta symbols. The dotted lines are for $z_{phot} = z_{spec} \pm 0.15 (1 + z_{spec})$. The fraction η of catastrophic outliers is defined as as fraction of galaxies for which $|z_{spec} - z_{phot}|/(1 + z_{spec}) > 0.15$ holds. $\sigma_{\Delta z/(1+z)}$ is a measure for the redshift accuracy, defined as $\sigma_{\Delta z/(1+z)} = 1.48 \times \text{median}(|z_{spec} - z_{phot}|/(1 + z_{spec}))$, applied to non-outliers only. This follows the definition of Ilbert et al. (2006). This ‘variance’ $\sigma_{\Delta z/(1+z)}$ equals 0.038 for the W1 and 0.035 for the W4 field. For this example we have been using the spectroscopic data to calibrate the zeropoint offsets.

Table 3. Photometric redshift accuracy separated for each sub-field (this makes use of the VVDS spectra only)

Field	$\sigma_{\Delta z/(1+z)}$	η [%]
W1p2p2	0.042	4.0
W1p2p3	0.038	4.0
W4m0m0	0.034	1.3
W4m0m1	0.030	2.8
W4m0m2	0.033	1.9
W4p1m0	0.034	0.7
W4p1m1	0.036	3.4
W4p1m2	0.043	2.1
W4p2m0	0.032	2.4
W4p2m1	0.037	3.0
W4p2m2	0.031	2.4

three from group old (old SEDs) to the other groups (younger SEDs) which has also been found by Ilbert et al. (2006).

It is worth to note, that the integration time eg. of the i' -band on the Deep Field D1 is > 35 times longer than integration time of the i' -band data in the Wide Field W1. Nevertheless, the outlier rate is only slightly larger and the accuracy is almost the same in the shallower sample (if one limits the comparison sample to $I < 22.5$). In other words: in order to obtain photometric redshifts for $I < 22.5$ galaxies, it does not play a role whether the data are ‘rather deep’ (W1, with $I < 24.5$) or ‘very deep’ (D1-T0003, with $I < 25.9$). For these depths the photon noise is not relevant any longer, but solely how well the templates can reproduce the true galaxy SEDs.

Table 4. Median redshifts in the three CFHTLS Wide Fields (columns) for samples selected according to $17.5 \leq i'_{AB} \leq 22$, $22 \leq i'_{AB} \leq 23$, $23 \leq i'_{AB} \leq 24$, and $24 \leq i'_{AB} \leq 25$ from the top to the bottom. Only galaxies with ‘good’ photometric redshifts are considered.

Magnitude interval	$z_{\text{median}}[\text{W1}]$	$z_{\text{median}}[\text{W3}]$	$z_{\text{median}}[\text{W4}]$
$17.5 \leq i'_{AB} \leq 22.0$	0.53	0.53	0.54
$22.0 \leq i'_{AB} \leq 23.0$	0.70	0.68	0.68
$23.0 \leq i'_{AB} \leq 24.0$	0.77	0.75	0.74
$24.0 \leq i'_{AB} \leq 25.0$	0.79	0.76	0.76

Table 5. Galaxy redshift distribution for objects with ‘good’ photometric redshifts in the CFHTLS Wide fields, using the parametrisation of Van Waerbeke et al. (2001).

Field	z_0	α	β
W1	0.84	2.2	2.4
W3	0.79	2.2	2.4
W4	0.80	2.2	2.4

6.3. Redshift distributions

Fig. 14 shows the galaxy redshift histogram of all objects in the four CFHTLS Wide Fields. The median redshift (see Tab. 4) is in good agreement in the four fields although the redshift distribution in the W1 field is shifted to higher redshift. In Fig. 15 the SED redshift distribution of all galaxies in the CFHTLS Wide Field W1 and W4 is shown. In Fig. 16 the galaxy redshift histogram of all objects in the CFHTLS Wide is shown.

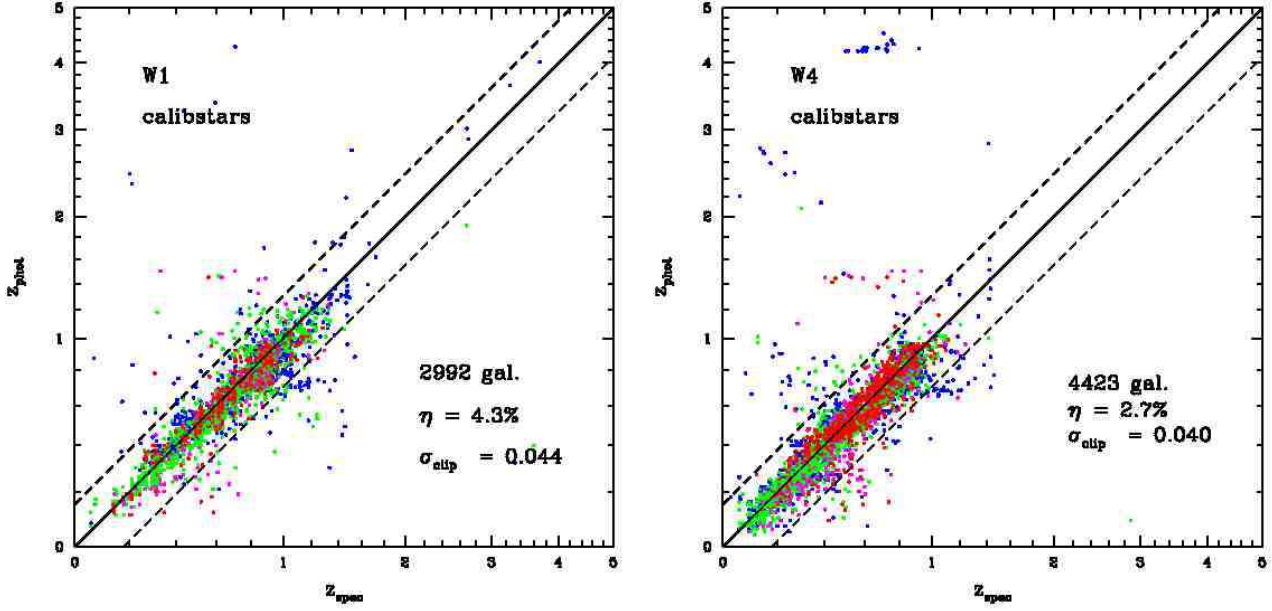


Fig. 11. Same as Fig. 9, this time we use the stellar colors and no spectroscopic information for the zeropoint calibration. The results become slightly worse/ Left panel: result for the CFHTLS W1 field. Right panel: result for the CFHTLS W4 field. Color coding for SED-types is as above.

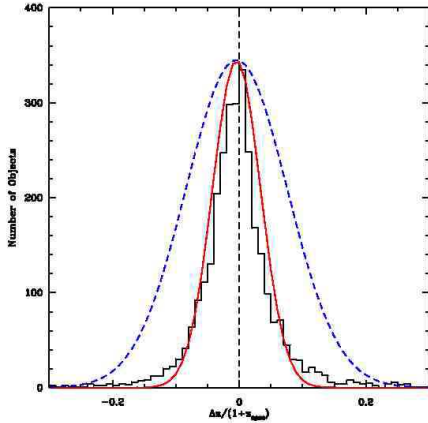


Fig. 7. Histogram of the photometric redshift errors in the CFHTLS Wide field W1. The median redshift error is -0.004 . The values for the formal dispersion and the clipped dispersion are $\sigma = 0.08$ and $\sigma_{\Delta z/(1+z)} = 0.038$ for the W1 field. The central distribution nearly is gaussian (with a width of 0.038) whereas the wings beyond $|z_{\text{phot}} - z_{\text{spec}}| > 0.1$ cannot be described with the same gaussian at all. To illustrate that, we have added two gaussians with width of 0.038 (in red) and 0.08 (dashed blue) and amplitudes matching the true error distribution at zero. The high formal dispersion of $\sigma = 0.08$ comes from the outliers; there are 27 objects with $|z_{\text{phot}} - z_{\text{spec}}| > 0.3$ and 16 objects with $|z_{\text{phot}} - z_{\text{spec}}| > 0.4$. Considering both $\sigma_{\Delta z/(1+z)}$ and σ tells, how ‘severe’ the outliers are.

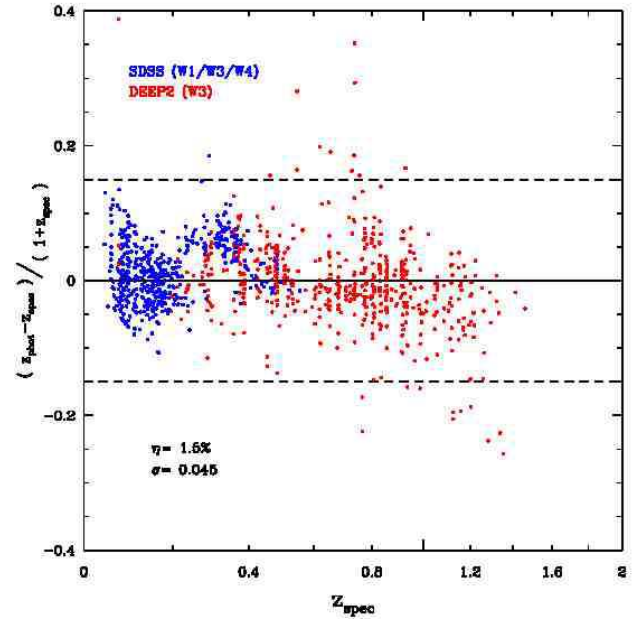


Fig. 10. Photometric redshifts in the CFHTLS Wide fields against the spectroscopic redshifts of the SDSS DR6 (blue dots) and DEEP2 (red dots). The dotted lines are for $z_{\text{phot}} = z_{\text{spec}} \pm 0.15(1+z_{\text{spec}})$. These spectroscopic data have not been used for the calibration of zeropoint shifts, and thus provide an independent estimate of the redshift accuracy.

The galaxy redshift distribution can be parameterized, following Van Waerbeke et al. (2001):

$$n(z_s) = \frac{\beta}{z_0 \Gamma\left(\frac{1+\alpha}{\beta}\right)} \left(\frac{z_s}{z_0}\right)^\alpha \exp\left[-\left(\frac{z_s}{z_0}\right)^\beta\right], \quad (5)$$

where (z_0, α, β) are free parameters. The best fitting values for the 3 fields (W1;W3;W4) are show in Table 6.3. It can be seen from median redshift that the three fields were observed to different depths.

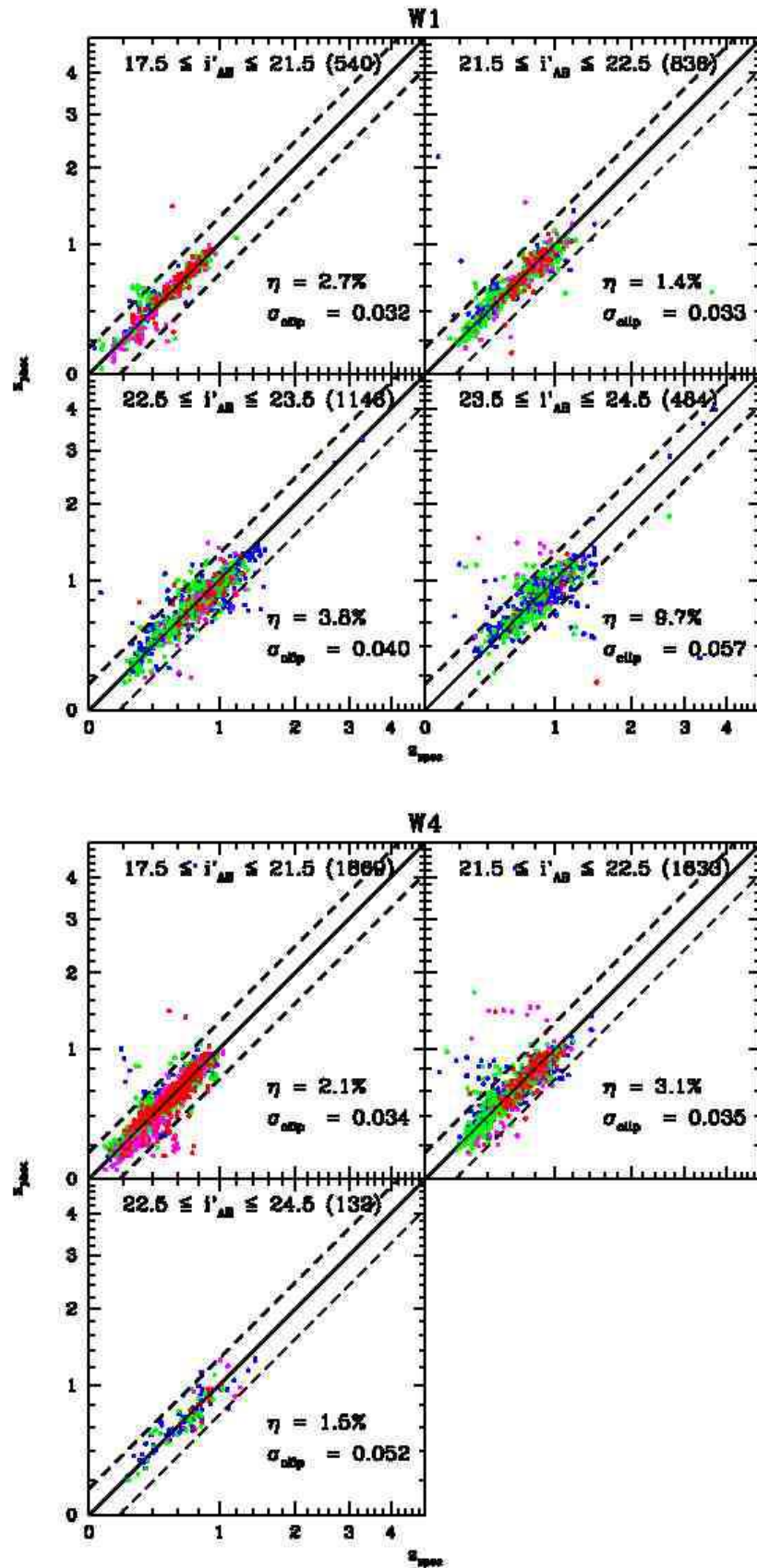


Fig. 12. Same as Fig. 9 (i.e., calibration on spectra). Each panel shows subsamples with different magnitudes. At the top the panels for the CFHTLS W1 field and at the bottom the CFHTLS W4 field are shown.

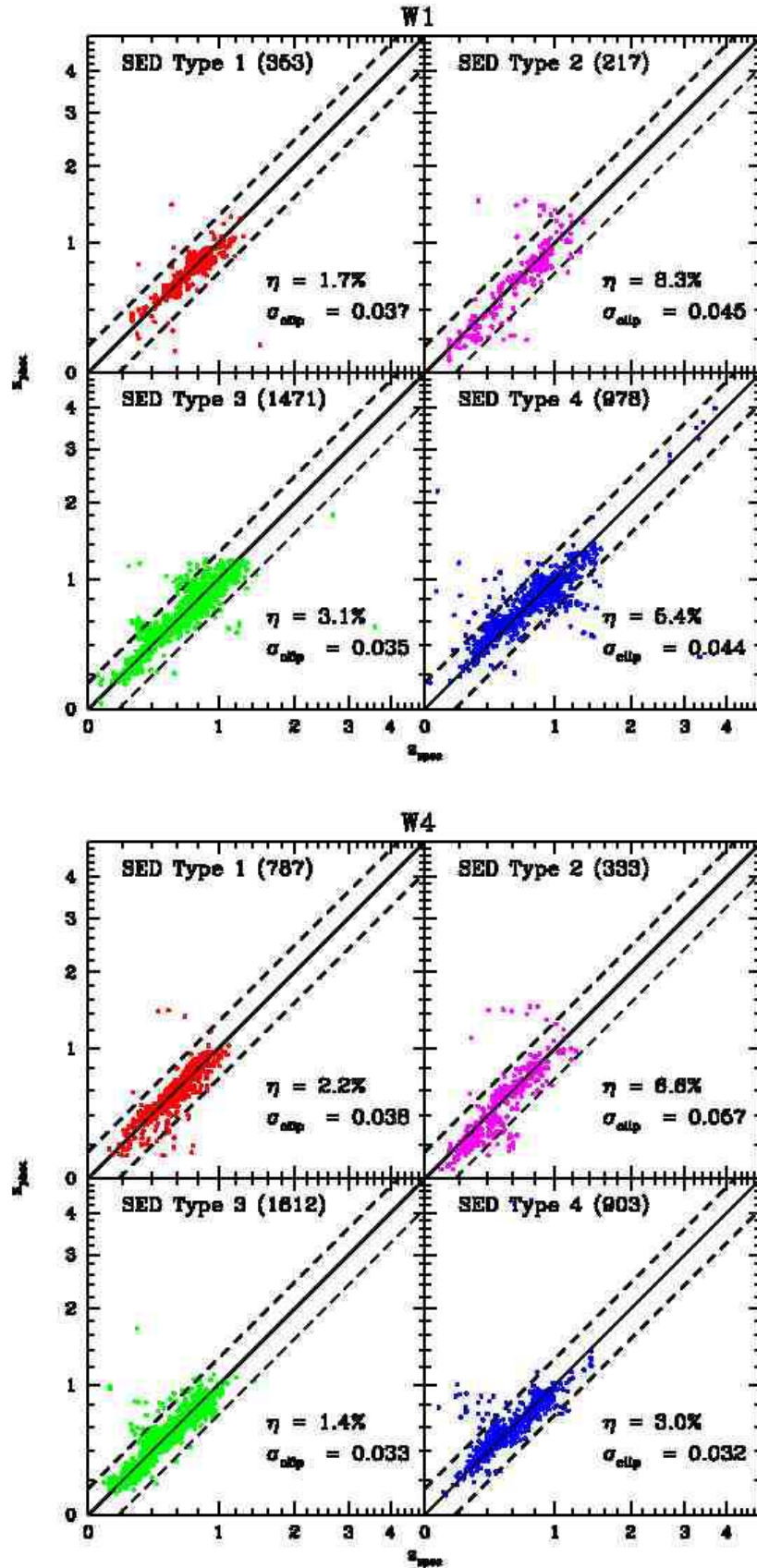


Fig. 13. Same as Fig. 9 (i.e., calibration on spectra). At the top panels the CFHTLS W1 field, selected at $17.5 \leq i_{AB} \leq 24$ and at the bottom panels the CFHTLS W4 field, selected at $17.5 \leq i_{AB} \leq 22.5$ is shown. Each panel shows a subgroup of galaxies which were sorted into four SED-groups according to the best-fitting template: The first group (red symbols) contains SEDs that describe ellipticals and S0s and is the fourth group (blue symbols) contains very blue, strongly starforming SEDs and the second (magenta symbols) and third (green symbols) group form a continuous sequence of SEDs in color and star forming activity between the first and fourth group.

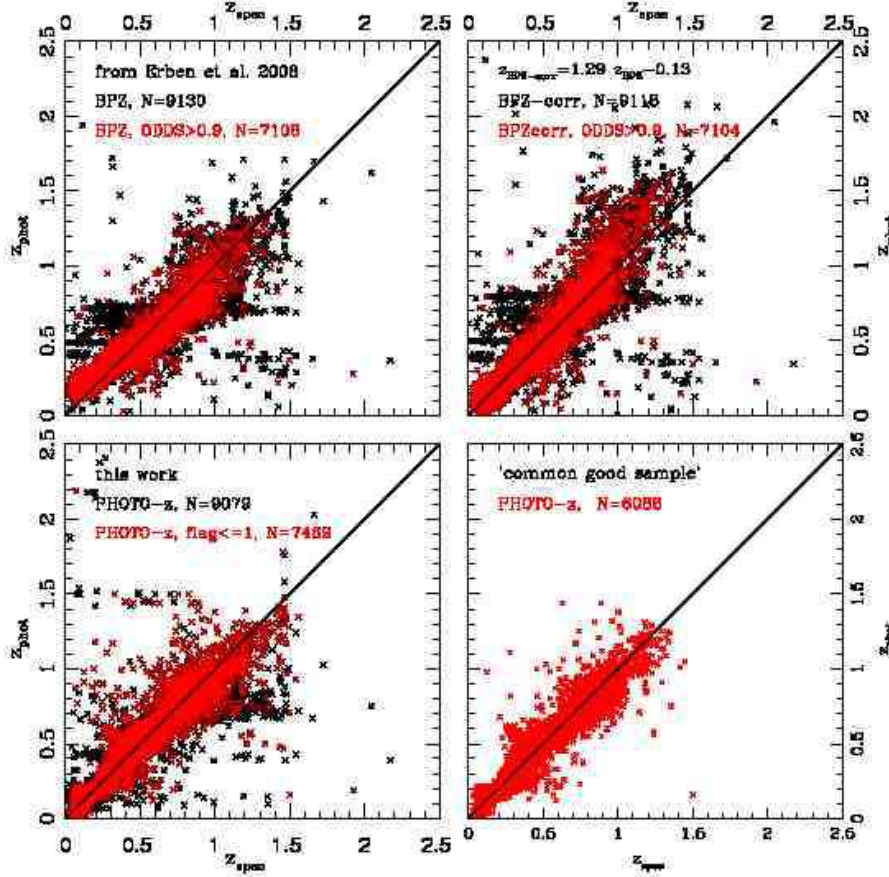


Fig. 17. This figure relates the spectroscopic and photometric redshifts for the BPZ-method (upper left), the bias corrected BPZ-redshifts (upper right) and the PHOTO-z redshifts of the Bender et al. (2001) code (lower left). In each case, the full sample is shown with black points, the sample which is considered as ‘good’ is shown with red points: these are in the case of the BPZ method all objects with $\text{ODDS} > 0.9$, and in the case of the PHOTO-z method all objects with $\Delta z_{\text{phot}} < 0.25 * (1 + z_{\text{phot}})$ after excluding starforming SEDs. The BPZ redshifts show a clear bias as reported in Erben et al. (2008) already. This bias is almost linear in redshift, and can be compensated for $z < 1.1$ with the equation given in the upper right panel. For higher redshift, this compensation leads to an overcorrection. The redshifts from the PHOTO-z code (lower left panel) are free of bias. They have a few more outliers, which is partly due to the fact, that there are more objects in this sample. At redshifts above 1.2 there might be a very small bias towards underestimating redshifts, there are, however, not many galaxies left. The lower right panel finally shows the photometric redshifts for the PHOTO-z method, were only objects that are considered as ‘good’ both in the BPZ, the BPZ-corrected and the PHOTO-z sample are shown. The exact criteria for the sample selection can be read off from Table 6.

7. Comparing CFHTLS-W photoz from different methods

In Erben et al. (2008) we had derived photometric redshifts with the BPZ algorithm. In this method the ‘ODDS’ output parameter of the BPZ method provides a very efficient way to disentangle likely accurate from likely inaccurate photometric redshift. We used an odds parameter of $\text{ODDS} = 0.9$ to select reliable redshifts and displayed the results for the reliable ones in Erben et al. (2008). The photo-z’s were systematically overestimated at low spectroscopic redshifts and underestimated at higher z . We have discussed potential origins of this bias already in Erben et al. (2008).

This trend has turned out to be very stable over all investigated fields with VVDS overlap (13 fields in total) and can be described as

$$z_{\text{BPZ-corr}} \approx 1.29 z_{\text{BPZ}} - 0.13 \quad (6)$$

Using this empirical relation (obtained from 13 fields) between the true redshift and the BPZ-photometric redshifts we can provide an alternative redshift estimate, which we call $z_{\text{BPZ-corr}}$.

We finally take all ‘reliable’ spectroscopic redshifts (VVDS, Deep and SDSS) and merge them with the photometric catalogs. Requiring a match in position within 0.56 arcseconds distances yields a combined catalog with photometric and spectroscopic redshifts for 9079 objects, 9130 objects and 9118 objects for the PHOTO-z, the BPZ- (from Erben et al. 2008) and the BPZ-corrected catalogs. Note, that the number of objects is not the same, because eg. PHOTO-z identifies likely stars (which are then removed from the sample) and some objects which have small redshifts in BPZ-catalog can obtain negative redshifts after applying the correction estimate from equation 7. We show the comparison of the spectroscopic and photometric redshifts in the W1, W3 and W4 fields in Fig. 17. Black points denote all objects in the sample, and red symbols are used, for objects, which a method flags as having ‘good’ or ‘reliable’ photomet-

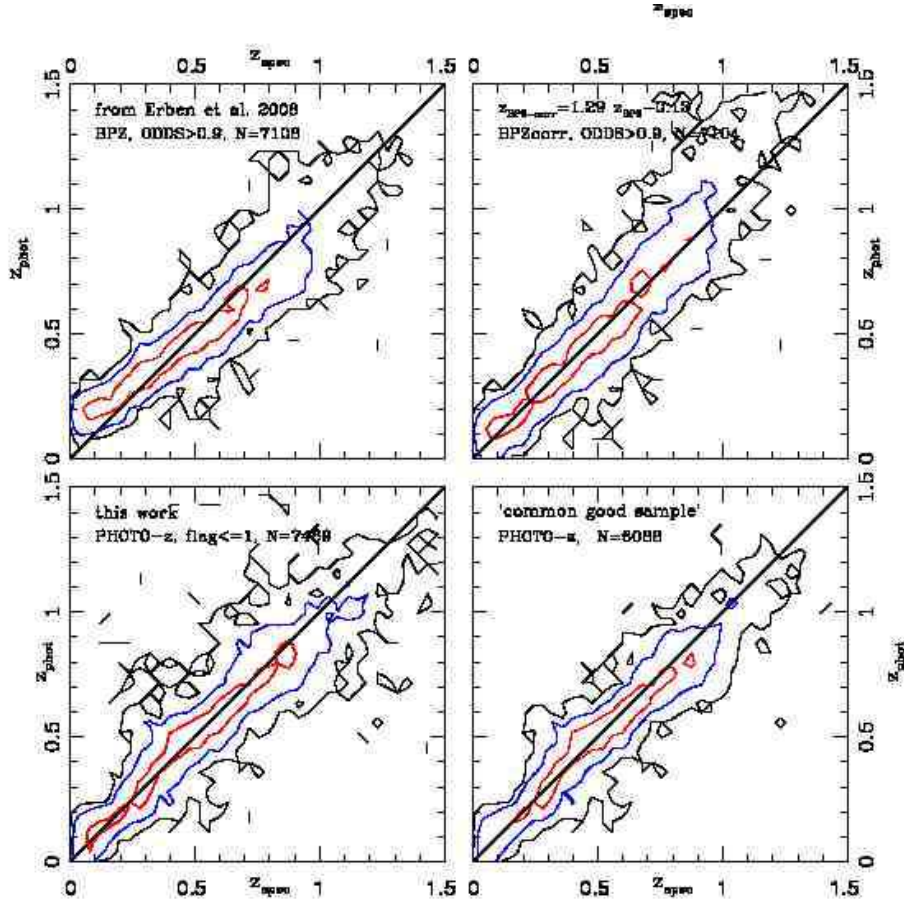


Fig. 18. Whereas the previous figure is intended to mostly show the location of outliers, one can see the density of objects in the spectroscopic-photometric redshift plane in this figure. The contour levels are chosen such that they contain 99 (black), 90 (blue) and 50 (red) percent of all galaxies with spectroscopic redshifts between zero and 1.5. As before the upper left, upper right and lower left panels are for the BPZ-method, the bias corrected BPZ-redshifts and the PHOTO-z redshifts of the Bender et al. code. The density distributions are obtained for the ‘good’ objects for each method only. The exact definition can be read in Table 6., the most relevant selection criterium can be seen in the figure itself. One can see again the bias in the BPZ photometric redshifts, the remaining bias at $z > 0.9 - 1$ for the BZP-corrected case, and that PHOTO-z method provides nearly bias free redshifts. If one uses only objects for which ‘good’ photozs can be obtained with all 3 methods and shows the result for the PHOTO-z values, one ends up with a fairly well behaved distribution, with small dispersion and outlier rate (see details in Table 6).

ric redshifts. In the overall sample, one sees a lot of systematics, most severely for the BPZ method (which is in the upper left panel). The relation for bias corrected BPZ redshifts and PHOTO-z redshifts are shown in the upper right and lower left panels. The PHOTO-z method has fewer systematics in the total galaxy sample shown (black points) than the BPZ method. Fig. 17 demonstrates that the ODDS parameter is very helpful in sorting out outliers (see red points in the upper panels of the same Figure). Fig. 18 shows the density distributions of points in the $z_{\text{true}} - z_{\text{photoz}}$ -space. The contours are isodensity contours, and their levels are chosen such that they contain 99 (black), 90 (blue) and 50 (red) percent of all objects which have true redshifts between zero and 1.5. Compared to the BPZ and BPZ-corrected redshifts, the PHOTO-z method shows hardly any bias. We also build that sample of objects which has ‘good’ redshifts with both the BPZ and PHOTO-z method, and show the comparison of true and PHOTO-z redshifts in the upper right subpanel of Fig. 18. These redshifts are bias free, have an outlier rate of only 1%, and in quality exceed the BPZ and BPZ-corrected redshifts according to Table 6.

This shows, that one can construct a subsample of objects with very robust photometric redshifts, which is useful for weak lensing studies. One should however try to keep the ‘good’ subsample as large as possible in order to have enough galaxies to measure the shapes. We therefore now compare the yield of ‘good’ objects with the PHOTO-z and BPZ-methods as a function of object magnitude for the photometric and spectroscopic sample. We use only objects from the W1p2p3-field (which are located in an area not flagged having potentially unreliable photometry, i.e. objects having a flag of zero in the photometric catalog) and show results in Fig. 20. The histogram for the number of objects with a given magnitude in the W1-field is shown in black in the upper two panels of this figure. The same histogram for objects which have spectroscopic data (and are not stars) in the W1-field is shown in black in the lower two panels. All objects (including stars) are shown as yellow histogram. One can see, that there are fairly many stars at the bright end. The histograms for those objects for which photometric redshifts could be derived and which are not classified as stars in terms of morphology or SED are shown in red, and those which have ‘good’ photometric

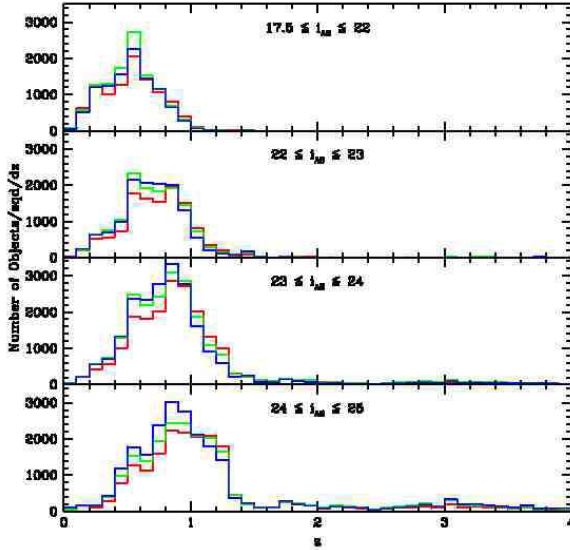


Fig. 14. Photometric redshift distributions of ‘good’ objects in the three CFHTLS Wide fields, W1 (red line), W3 (blue line) and W4 (green line). The redshift distributions are shown from bright to faint selected samples.

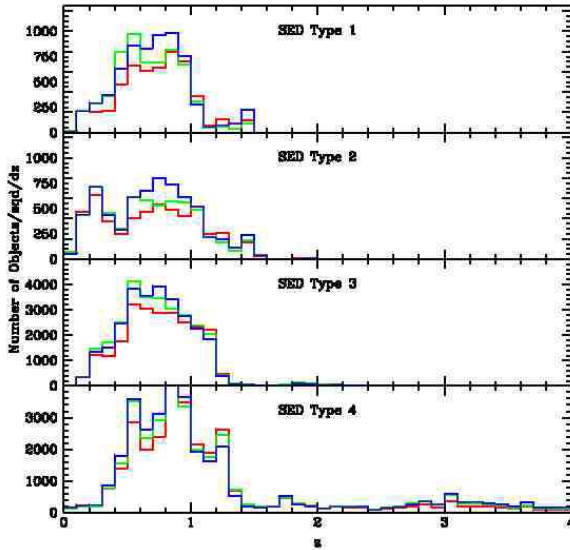


Fig. 15. Same as Fig. 14, but each panel shows a different selection of spectral types, according to the best-fitting template. From top to the bottom: The first group contains SEDs that describe ellipticals and S0s and the fourth group contains very blue, strongly starforming SEDs; the second and third group form a continuous sequence of SEDs in color and star forming activity between the first and fourth group.

redshifts are shown in green. The left panels are for PHOTO-z redshifts, the right panels are for BPZ-redshifts. One can see, that the yield of ‘good’ objects is quite complete for the spectroscopic and photometric sample for both the PHOTO-z and BPZ-method up to $i' = 22$. For fainter magnitudes the BPZ-method is less complete: one obtains good redshifts for objects brighter

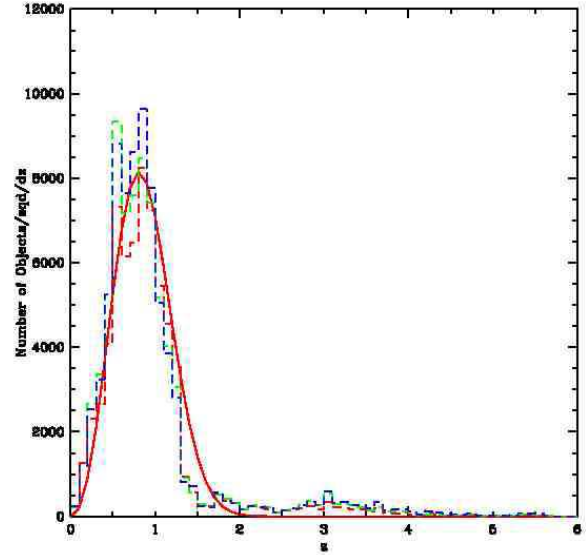


Fig. 16. Redshift number distributions for galaxies in the three CFHTLS Wide fields. The distributions are red, blue and green for the W1, W3 and W4 fields, the median redshifts in these fields are $z_{median,W1} = 0.84$, $z_{median,W3} = 0.79$ and $z_{median,W4} = 0.80$. The red solid curve is a fit to the mean galaxy distribution for the W1-field using the parametric description given, e.g., in Van Warbeke et al. (2001).

than $i' = 24.5$ only for 54 percent of all objects using BPZ. For the PHOTO-z method, this ratio equals 70 percent.

We are aware that the fraction of galaxies which have ‘good’ photometric redshifts (low clipped dispersion and low outlier rate) should be increased, or become ‘identical’ to the original sample. This can be achieved by adding NIR data, by improving our SED-templates, and probably more important by making our photometry (including the convolution to the same PSF) more accurate. This will be subject of a further study.

8. Summary

We tested the performance of the photometric redshift code of Bender et al. (2001) with the CFHT-MegaCam filter system using the CFHTLS D1 data. The comparison of our photometric redshift results with spectroscopic data and photometric redshift results from Ilbert et al. (2006) shows: our performance is very close to that of Ilbert et al. (2006), although we use only about half of the optical bands (and no NIR data). This makes us confident that results we then derived for the CFHTLS-Wide fields are reliable.

We analyzed the CFHTLS-Wide data and showed that the colors of stars can be measured accurately enough and that the throughput of the system is known well enough to allow relative zero point calibration for the $g'r'i'z'$ bands using the colors predicted from Pickles library stars. We could not match the color-color diagrams on the Pickles-library-star colors when the u^* -band is involved. We nevertheless found out, that calibrating zeropoints such that the $u^* - g'$ colors approximately match at the red end, gives results which describe the galaxy colors correctly. In this case the likely reason for the mismatch would be that Pickles stars are metal enriched and do not show the UV excess of metal poor halo stars.

Table 6. Photometric redshifts of PHOTO-z, BPZ and BPZ-corr in the W1, W3 and W4 fields are compared to the spectroscopic sample consisting of VVDS, DEEP2, SDSS DR6 spectroscopic data. In this table, σ denotes the ‘true’ dispersion, without clipping outliers, and σ_{clip} denotes the width of the distributions after clipping $\Delta z_{\text{photoz}} > 0.25 * (1 + z_{\text{photoz}})$ outliers (as defined in equation 3 and introduced by Ilbert et al. 2006).

Code	Sample: CFHTLS-W1,	$N_{z_{\text{spec}}}$	Median-error	Mean-error	σ	σ_{clip}	η [%]
PHOTO-z	all objects	9079	-0.0036	0.0065	0.158	0.040	5.7%
PHOTO-z	good PHOTO-z objects	7469	-0.0025	0.0019	0.071	0.038	2.8%
PHOTO-z	common good objects	6088	-0.0025	0.0001	0.053	0.037	1.0%
BPZ	all objects	9130	-0.0005	0.0257	0.194	0.056	10.5%
BPZ	good BPZ objects	7108	-0.0017	0.0013	0.066	0.054	2.7%
BPZ	common good objects	6088	-0.0050	0.0000	0.062	0.056	1.5%
BPZ _{corr}	all objects	9118	+0.0076	0.0414	0.241	0.051	11.0%
BPZ _{corr}	good BPZ objects	7104	+0.0024	0.0055	0.065	0.047	2.7%
BPZ _{corr}	common good objects	6088	+0.0063	0.0098	0.060	0.048	1.8%

The samples are defined as follows:

all PHOTO-z objects: $z_{\text{spec}} > 0, z_{\text{PHOTO-z}} > 0$

good PHOTO-z objects: $z_{\text{spec}} > 0, z_{\text{PHOTO-z}} > 0, \text{flag}_{\text{PHOTO-z}} \leq 1$

common good objects: $z_{\text{spec}} > 0, z_{\text{PHOTO-z}} > 0, z_{\text{BPZ}} > 0, z_{\text{BPZ-corr}} > 0, \text{flag}_{\text{PHOTO-z}} \leq 1, \text{ODDS}_{\text{BPZ}} > 0.9$

all BPZ- objects: $z_{\text{spec}} > 0, z_{\text{BPZ}} > 0$

good BPZ objects: $z_{\text{spec}} > 0, z_{\text{BPZ}} > 0, \text{ODDS}_{\text{BPZ}} > 0.9$

all BPZ-corr objects: $z_{\text{spec}} > 0, z_{\text{BPZ-corr}} > 0$

good BPZ-corr objects: $z_{\text{spec}} > 0, z_{\text{BPZ-corr}} > 0, \text{ODDS}_{\text{BPZ}} > 0.9$

After the improved relative zeropoint calibration we derived photometric redshifts for 2.5 million of galaxies. We identified galaxies with likely inaccurate redshifts as those which have formally a large photometric redshift error (as provided by the code) and which have SEDs which are likely to be mismatched with another SED at different redshifts. By flagging those objects we end up with a sample of galaxies with fairly precise photometric redshifts. We investigated the redshift accuracy as a function of brightness and SED-type, and find similar results (in numbers and in trend) as Ilbert et al. (2006) for CFHTLS-Deep data set.

The overall photometric redshift precision was quantified by comparing all W1, W3 and W4 photometric redshifts to VVDS, DEEP2 and SDSS spectra. We then also investigated the BPZ-redshifts from Erben et al. (2008). These redshifts are biased, and can be corrected according to $z_{\text{BPZ-corr}} = 1.29 z_{\text{BPZ}} - 0.13$. This correction slightly overcorrects at redshifts larger than 1. We then analyzed all three photometric redshifts samples (PHOTO-z, BPZ, BPZ-corr) in more detail: Taking all objects (irrespective of photoz quality flags) the outlier-rate varies between 10 percent (BPZ/BPZ-corr) and 6 percent (PHOTO-z). If we select only good objects (using photometric redshift errors and SED types for the PHOTO-z method and using the ODDS parameter for the BPZ method) we can reduce the outlier rate to about 2.7 percent for all three catalogs. The width of the distributions (after clipping) then becomes 0.038, 0.054 and 0.057 for the PHOTO-z, the BPZ and the BPZ-corr catalogs. The width of the (unclipped) distribution is 0.071 (PHOTO-z) and 0.066 (BPZ/BPZ-corr).

Finally we consider only galaxies which are classified as ‘reliable’ objects in all three catalogs, and investigate the photometric redshift quality for this ‘common sample’. We indeed can reduce the outlier rate to 1 percent (PHOTO-z) and 1.5 to 1.8 percent for the BPZ-versions. The width of the distributions (after clipping) then becomes 0.037, 0.056 and 0.058 for the PHOTO-z, the BPZ and the BPZ-corr catalogs. The width of the (unclipped) distribution is 0.05 (PHOTO-z) and 0.06 (BPZ/BPZ-corr).

We conclude that this common sample defines a high quality redshift sample, which has (in the case of PHOTO-z) no bias and a very low outlier rate. This sample is ideally suited for weak lensing analysis like growth of cosmic shear and in particular the shear ratio test behind clusters of galaxies. Since these ‘good’ redshift samples include several selections steps, and are fairly incomplete at faint magnitudes we don’t recommend this sample to be taken for galaxy evolution studies in general.

The original sample (all galaxies) can be taken for that, which however requires to understand the impact of outliers (eg. on derived luminosity functions, galaxy colors as a function of redshift and environment density);

We are currently working on increasing the ‘good’ sample, or decreasing the outlier rate of the ‘remaining’ sample, to finally unite them to one again. Goal is to obtain a ‘complete sample’ with outlier rates as low as 2 percent. This requires a more detailed study of photometric calibration, improved convolution for more precise aperture colors, improved SEDs, potentially varying priors, and including further colors where possible.

We provide these catalogs (with future updates and extensions) on request.

Acknowledgements. We are grateful to the Terapix consortium for developing and providing tools for the handling of large CCD images in general, and for the image processing and pipeline software for MegaCam, and finally for the production of photometrically and astrometrically corrected images within the CFHTLS survey. This work uses images which have been compared to the CFHTL T0003 release when deriving the photometric and astrometric accuracy.

We acknowledge use of the Canadian Astronomy Data Centre, which is operated by the Dominion Astrophysical Observatory for the National Research Council of Canada’s Herzberg Institute of Astrophysics.

We thank Y. Mellier and J. Coupon for the friendly spirit in which the Munich and Paris teams independently worked on their photometric redshifts.

This work was supported by the DFG Sonderforschungsbereich 375 ‘Astro-Teilchenphysik’, the DFG priority program 1177 (Se1038), TRR33 ‘The Dark Universe’ and the DFG ‘Cluster of Excellence on the Origin and Structure of the Universe’.

We all, in particular M. L., thank the European Community for the support by the Marie Curie research training network ‘DUEL’. M.L. further thanks the University of Bonn and the University of British Columbia for hospitality.

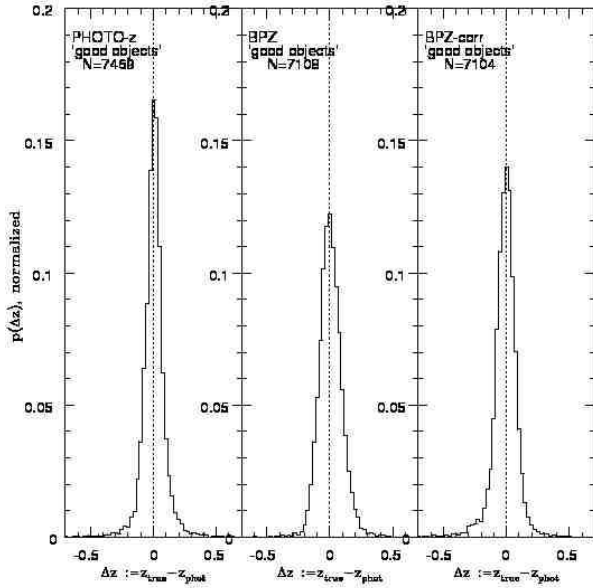


Fig. 19. This figure shows normalized histograms for the photometric redshift error, $\Delta z = z_{\text{true}} - z_{\text{photoz}}$ for the PHOTO-z method (left panel), for the BPZ-method (middle panel) and for the BPZ-(bias) corrected catalogs (right panel), using the W1, W2, and W3 field and all reliable spectroscopic VVDS, DEEP2 and SDSS redshift data. Redshift biases as seen in the BPZ catalog don't show up in this histogram (which combines all spectroscopic redshifts up to $z = 4.5$) since only the histograms within small redshift slices are shifted relative to $\Delta z = 0$. One can see, however, that the PHOTO-z redshifts have more objects with redshifts very close to the true redshift relatively to the other two methods (note, that these histograms are normalized). In addition to that, the PHOTO-z method provides the largest amount of galaxies in its 'good' sample.

References

- Adelman-McCarthy, J. K., Agüeros, M. A., Allam, S. S., et al. 2007, *ApJS*, 172, 634
 Arnouts, S., Cristiani, S., Moscardini, L. et al. 1999, *MNRAS*, 310, 540
 Bahcall, N. A. & Soneira, R. M. 1983, *ApJ*, 270, 20
 Bender, R., Appenzeller, I., Böhm, A., et al. 2001, Proceedings of the ESO Workshop held at Garching, Germany, 9-12 October 2000
 Benítez, N. 2000, *ApJ*, 536, 571
 Bolzonella, M., Miralles, J.-M., Pello, R. 2000, *A&A*, 364, 476
 Brunner, R. J., Connolly, A. J., Szalay, A. S., et al. 1997, *ApJ*, 482, 21
 Bruzual, G., Charlot, S., 2003, *MNRAS*, 344, 1000
 Calzetti, D., Kinney, A. L., Storchi-Bergmann, T. 2000, *ApJ*, 553, 682
 Calzetti, D., Kinney, A. L., Storchi-Bergmann, T. 1994, *ApJ*, 429, 582
 CWW - Colman, G. D., Wu, C.-C., Weedman, D. W. 1980, *ApJS*, 43, 393
 Colless, M., Dalton, G., Maddox, S., et al. 2001, *MNRAS*, 328, 1039
 Collister, A. A. & Lahav, O. 2004, *PASP*, 116, 345
 Connolly, A. J., Szalay, A. S., Bershady, M. A., et al. 1995, *AJ*, 110, 107
 Davis, M., Faber, S. M., Newman, J., et al. 2003, *SPIE*, 4824, 161
 Davis, M., Guhathakurta, P., Konidaris, N. P., et al. 2007, *ApJ*, 660, L1
 Drory, N., Feulner, G., Bender, R., Botzler, C., et al. 2001, *MNRAS*, 325, 550
 Erben, T., Schirmer, M., Dietrich, J., et al. 2005, *AN*, 326, 432
 Erben, T., Hildebrandt, H., Lerchster, M., et al. 2008, *A&A*, submitted
 Feldmann, R., Carollo, C. M., Porciani, C., et al. 2006, *MNRAS*, 372, 565
 Ferguson, H., Dickinson, M., Williams, 2000, *ARA&A*, 38, 667
 Fernandez-Soto, A., Lanzetta, K. M., Yahil, A., 1999, *ApJ*, 513, 34
 Feulner, G., Hopp, U., Botzler, C. S. 2006, *A&A*, 451, 13
 Feulner, G., Goranova, Y., Drory, N., et al. 2005, *ApJ*, 633, 9
 Gabasch, A., Goranova, Y., Hopp, U., et al. 2007, astro-ph 0710.5244
 Gabasch, A., Hopp, U., Feulner, G., et al. 2006, *A&A*, 448, 101
 Gabasch, A., Salvato, M., Saglia, R., et al. 2004, *ApJ*, 616, 83

- Gabasch, A., Bender, R., Seitz, S., et al. 2004, *A&A*, 441, 41
 Garilli, B., Maccagni, D., Le Brun, V., et al. 2007, *A&A*, submitted
 Gwyn, S. D. J. & Hartwick, F. D. A. 1996, *ApJ*, 468, 77
 Hildebrandt, H., Wolf, C., Benitez, N. 2008, *A&A*, 480, 703
 Hildebrandt, H., Erben, T., Schirmer, M., et al. 2007, astro-ph 0705.0438
 Ilbert, O., Arnouts, S., McCracken, H. J., et al. 2006, *A&A*, 457, 841
 Jarrett, T.-H., Chester, T., Cutri, R., et al. 2000, *AJ*, 119, 2498
 Kennicutt, R. C. 1992, *ApJS*, 79, 255
 Kerscher, M., Szapudi, I., and Szalay, A. S. 2000, *ApJ*, 535, L13
 Koo, D. C. 1985, *AJ*, 90, 418
 Lanzetta, K. M., Yahil, A., Fernandez-Soto, A. 1996, *Nature*, 381, 759
 Landy, S., and Szalay, A. S. 1993, *ApJ*, 421, 64
 Le Fèvre, O., Vettolani, G., Bottini, D., et al. 2005, *A&A*, 439, 845
 Le Fèvre, O., Mellier, Y., McCracken, H.J., et al. 2004, *A&A*, 417, 839
 Maraston, C. 1998, *MNRAS*, 300, 872
 Madau, P. 1995, *ApJ*, 441, 18
 Mandelbaum, R., Seljak, U., Hirata, C. M., et al. 2007, astro-ph 07091692
 McCracken, H. J., Radovich, M., Bertin, E., et al. 2003, *A&A*, 410, 17
 Mobasher, B., Capak, P., Scoville, N. Z., et al. 2007, *ApJS*, 172, 117
 Niemack, M. D., Jimenez, R. Verde, L., et al. 2008, astro-ph 0803.3221
 Peebles, P. J. E. 1980, Princeton University Press, 1980. 435 p.
 Pello, R., Miralles, J. M., Le Borgne, J.-F., et al. 1996, *A&A*, 314, 73
 Pickles, A. J., 1998, *PASP*, 110, 863
 Sawicki, M. J., Yee, H. K. C., Lin, H. 1997, *JRASC*, 90, 337
 Schneider, M., Knox, L., Zhan, H. and Connolly, A. 2006, *ApJ*, 651, 14
 Stoughton, C., Lupton, R. H., Bernardi, M., et al. 2002, *AJ*, 123, 3487
 Tagliaferri, G., Longo, G., Andreon, S., et al. 2002, astro-ph 0203445
 Van Waerbeke, L., Mellier, Y., Radovich, M., et al. 2001, *A&A*, 374, 757
 Weiner, B. J., Phillips, A. C., Faber, S. M., et al. 2005, *ApJ*, 620, 595
 Williams, R. E., Blacker, B., Dickinson, M., et al. 1996, *AJ*, 112, 1355
 Wolf, C., Meisenheimer, K., Kleinheinrich, M., et al. 2004, *A&A*, 421, 913
 Wang, Y., Bahcall, N., Turner, E. L. 1998, *AJ*, 116, 2081
 Vogt, N., Koo, D., Phillips, A. C., et al. 2005, *ApJS*, 159, 41
 Yee, H. K. C. 1998, astro-ph 9809347

Appendix A: Details on the photometric redshift redshift catalog

Using the notation introduced in Erben et al. (2008), we briefly explain the most important FITS keys in the multi-color catalogs in the Table A.1 .

Table A.1. Description of the most important FITS keys in the CARS multi-color catalogs. The ASCII catalog version contains one aperture magnitude at a diameter of $1''.86$.

key name	description	measured on
SeqNr	Running object number	-
ALPHA_J2000	Right ascension	unconvolved <i>i</i> -band image
DELTA_J2000	Declination	unconvolved <i>i</i> -band image
Xpos	x pixel position	unconvolved <i>i</i> -band image
Ypos	y pixel position	unconvolved <i>i</i> -band image
FWHM_WORLD	FWHM assuming a Gaussian core	unconvolved <i>i</i> -band image
FLUX_RADIUS	half-light-radius	unconvolved <i>i</i> -band image
A_WORLD	profile RMS along major axis	unconvolved <i>i</i> -band image
B_WORLD	profile RMS along minor axis	unconvolved <i>i</i> -band image
THETA_WORLD	position angle	unconvolved <i>i</i> -band image
Flag	SExtractor extraction flags	unconvolved <i>i</i> -band image
CLASS_STAR	star-galaxy classifier	unconvolved <i>i</i> -band image
MAG_AUTO	total <i>i</i> -band magnitude	unconvolved <i>i</i> -band image
MAGERR_AUTO	total <i>i</i> -band magnitude error	unconvolved <i>i</i> -band image
MAG_ISO_x ^a	isophotal magnitude in x-band	PSF-equalised x-band image
MAGERR_ISO_x	isophotal magnitude error in x-band	PSF-equalised x-band image
MAG_APER_x	aperture magnitude vector in x-band	PSF-equalised x-band image
MAGERR_APER_x	aperture magnitude error vector in x-band	PSF-equalised x-band image
MAG_LIM_x	limiting magnitude in x-band	unconvolved x-band image
FLUX_ISO_x	isophotal flux in x-band	PSF-equalised x-band image
FLUXERR_ISO_x	isophotal flux error in x-band	PSF-equalised x-band image
FLUX_APER_x	aperture flux vector in x-band	PSF-equalised x-band image
FLUXERR_APER_x	aperture flux error vector in x-band	PSF-equalised x-band image
Z1_PHOT	photometric redshift best-fit SED	-
ERR_Z1_PHOT	error of photometric redshift best-fit SED	-
SED_TYPE	SED type	-
Flag_PHOT	global photometric redshift flag key ^b	-
MASK	global mask key ^c	-

^a $x \in [u, g, r, i, z]$ ^b 1 = object FWHM < PSF, 2 = $\Delta z > 0.25 * (1 + z)$, 4 = ext. flag (SExtractor, absolute photometry) for object, 8 = SED rejected, 16 = star SED, 32 = no photometric redshift, and combinations.^c 0 for objects inside masks and 1 otherwise

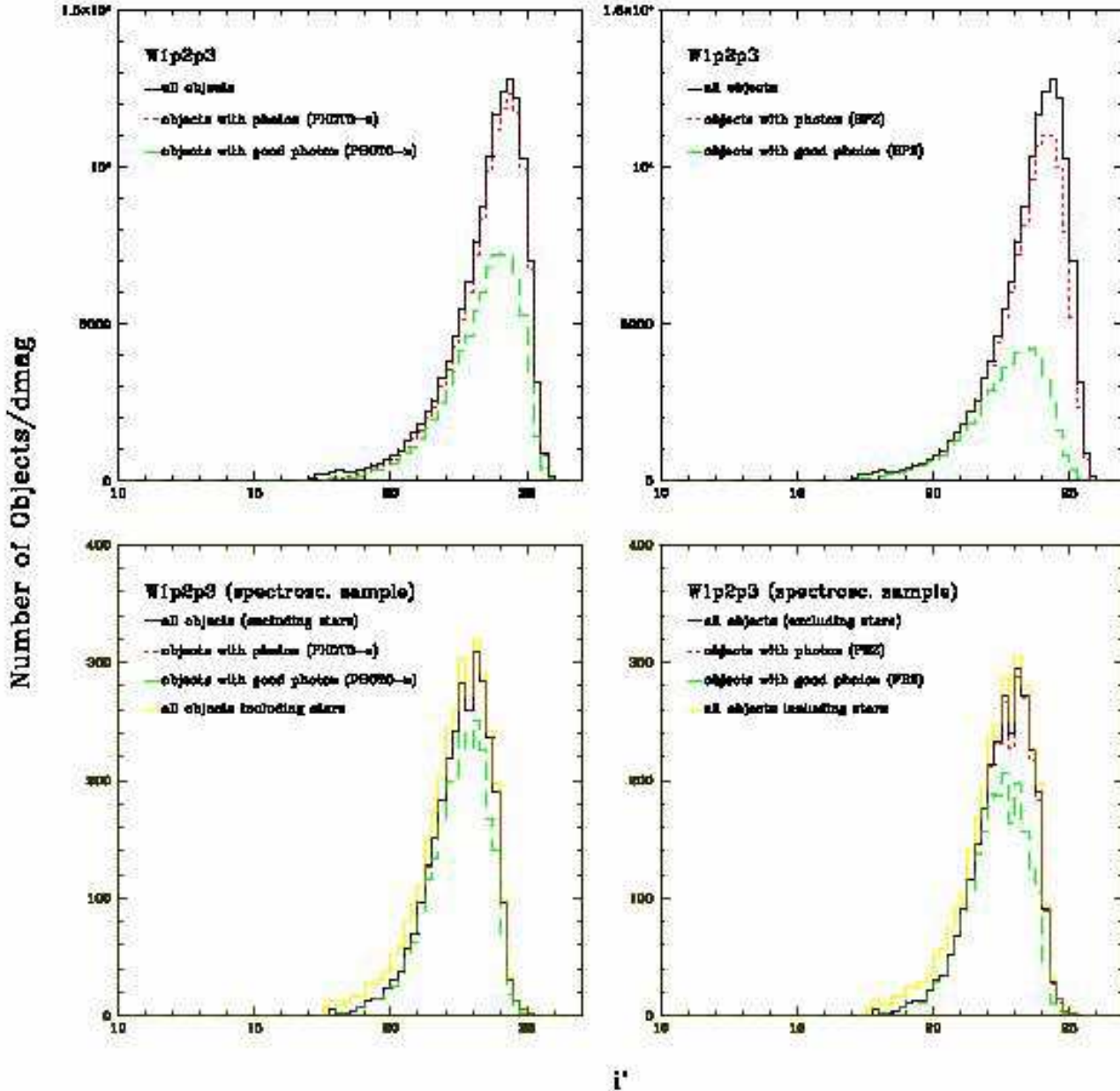


Fig. 20. This figure shows the number of objects in the W1p2p3 field as a function of magnitude. The upper two panels are for the photometric catalog, the lower two panels are for the spectroscopic catalog (from the VVDS data). Black color is used for the full photometric and spectroscopic galaxy catalog. (The yellow histograms for the spectroscopic sample in addition also contain stars). The red histograms are for those objects, for which photometric redshifts could be obtained, and which are not characterized as stars by their photometry or morphology. One sees, that the stars are properly selected out from the spectroscopic data set, by their photometric and morphological parameters already – even if the spectra were not there. The green histograms are for those objects which are flagged as ‘good’ objects, i.e. which are expected to have secure photometric redshifts. One can see, that the PHOTO-z method (two left panels) can provide a larger fraction of galaxies with reliable redshifts than the BPZ-method (two right panels). If one considers objects to a limiting magnitude of $i' = 24.5$ (which are at the same time outside any eg. bright star mask) one obtains for 70 percent of all objects a ‘good’ photometric redshift with PHOTO-z. For the BPZ-redshifts this is the case for only 54 percent of all objects (for $i' < 24.5$).